

DEVELOPMENT OF MULTI-SCALE
COMPUTATIONAL TOOLS FOR THE STUDY OF
INTERFACES

A Dissertation

Presented to the Faculty of the Graduate School

of Cornell University

in Partial Fulfillment of the Requirements for the Degree of

Doctor of Philosophy

by

Kiran Mathew

February 2016

© 2016 Kiran Mathew
ALL RIGHTS RESERVED

DEVELOPMENT OF MULTI-SCALE COMPUTATIONAL TOOLS FOR THE
STUDY OF INTERFACES

Kiran Mathew, Ph.D.

Cornell University 2016

Interfaces play a pivotal role in modern devices and applications. A proper understanding of them requires an approach that supplements the experimental studies with appropriate computational undertakings. Computational methodologies and tools play a major role in the enhancement of the understanding of existing as well as newly discovered technologies. Since a unified theory/-software tool that describes all encompassing phenomena does not yet exist, a variety of models/tools that deals with various phenomena at a range of length and time scales need to be considered. This calls for the development of combined models that are computationally efficient and scientifically accurate to describe the length and time scales relevant to the processes in the systems of interest. This thesis describes the development and the implementation of such combined methods/tools for the simulation and analysis of a variety of interfacial systems.

The first part of this thesis presents the development and implementation of efficient implicit solvation models to describe solid-liquid interfaces in the density-functional theory (DFT) framework and its implementation in the widely used DFT code Vienna Ab-initio Software Package (VASP). This is followed by the description of the development of an open-source high-throughput framework for the creation, screening, simulation, and analysis of interfacial systems. The high-throughput framework enables the creation

of various interfacial structures such as solid/liquid interfaces, nanocrystal/ligands and heterostructure interfaces. The framework also enables the generation of input files for various DFT/MD softwares so that an in depth analysis of the screened interfaces at different length scales can be done if desired. The open-source tools developed as part of this work are made freely available and some have already become part of widely used scientific software packages such as the VASP DFT code.

BIOGRAPHICAL SKETCH

Kiran Mathew was born in Kerala, India in 1986. He received his bachelors degree in Aerospace Engineering from the Indian Institute of Technology, Kanpur, India in 2008 and subsequently joined the PhD program at Cornell University. Following a brief stint in the Department of Mechanical and Aerospace Engineering he switched to the Department of Materials science and Engineering in 2010 to pursue his PhD under the supervision of Dr. Richard Hennig. Under Dr. Hennig's guidance he worked primarily on developing methodologies and software tools to study various aspects of materials interfaces. During this period, he initiated the development of the open-source solvation framework, VASPsol, for the widely used DFT software VASP. It is currently the default and the only solvation framework available in VASP. He also initiated another open-source project, MPInterfaces, for the high throughput screening of interfaces.

To my family.

ACKNOWLEDGEMENTS

First and foremost, I would like to thank my adviser Dr. Richard Hennig for the guidance and support that he has provided me through out the course of my PhD. Coming from an Aerospace Engineering background, his immense support has really made the transition to the Materials Science easy for me. During the initial period of my PhD while I was fumbling with the projects, he had been extremely patient with me and kept my morale high with his highly contagious optimism. The years that I have spent in his group have been a really transformative period for me. The range of skills that I have acquired over the course of phd would not have been possible If I hadn't been working with him.

I would like to express my gratitude towards Dr. Richard Robinson and Dr. Robert Van Dover for serving on my committee, for their constructive criticisms on my work through the a-exam questions and for supporting me by being my references. I am also grateful to Dr. Richard Hennig and Dr. Susan Sinnot for the advise and the support that they provided while job searching.

I would also like to acknowledge the funding resources, the Energy Materials Center Cornell (EMC2) and the National Science Foundation (NSF), that made this research work possible. None of this work would have been possible without the generous amount of computational resources made available by XSEDE and Hipergator.

The fun time I had with the friends in the group, especially the BBQs, late night poker sessions as well as argument sessions, will always stay with me. I also like to thank my new friends at UF for welcoming me with open arms and for making the brief stay utmost pleasurable and productive.

Last but not the least, I am extremely grateful to my parents and sister for being their for me and supporting me unconditionally throughout the years.

My parents have played a significant role in directing me to a career in science. This PhD would not have been possible without their encouragement and the fostering environment that they provided me to pursue my ever fluctuating interests.

TABLE OF CONTENTS

Biographical Sketch	iii
Dedication	iv
Acknowledgements	v
Table of Contents	vii
List of Tables	ix
List of Figures	x
1 Introduction	1
1.1 Importance of solid/liquid interfaces	1
1.2 Computational approaches for multiscale modeling	5
1.2.1 Electronic structure methods	6
1.2.2 High-throughput framework for screening interfaces	15
2 Self-consistent linear solvation model in plane-wave density-functional theory ¹	17
2.1 Abstract	17
2.2 Introduction	17
2.3 Theoretical framework of implicit solvation model	20
2.4 Implementation of implicit solvation model	28
2.5 Validation of implicit solvation model	32
2.6 Applications	34
2.6.1 Solvation effects on metal and semiconductor nanocrystals	35
2.6.2 Reaction pathways	37
2.7 Conclusions	39
3 Implicit self-consistent description of electrolyte in plane-wave density-functional theory ²	41
3.1 Abstract	41
3.2 Introduction	41
3.3 Theoretical framework	44
3.3.1 Total energy	44
3.3.2 Minimization	47
3.4 Implementation and validation	48
3.5 Applications	51
3.6 Conclusions	53

¹Published as 'Kiran Mathew, R. Sundararaman, K. Letchworth-Weaver, T. A. Arias, and R. G. Hennig, *J. Chem. Phys.*, 140(8):084106, 2014'

²To be published as 'Kiran Mathew and R. G. Hennig, Implicit self-consistent description of electrolyte in plane-wave density-functional theory'

4	Self-consistent non-linear solvation model in plane-wave density-functional theory ³	54
4.1	Abstract	54
4.2	Introduction	54
4.3	Theoretical framework	57
4.3.1	Total energy	57
4.3.2	Self-consistent minimization	61
4.4	Implementation and validation	65
4.5	Applications	67
4.6	Conclusions	68
5	High-throughput Screening of interfaces ⁴	69
5.1	Abstract	69
5.2	Introduction	69
5.3	MPInterfaces: Overview with examples	71
5.3.1	Ligand capped nanoparticles	72
5.3.2	Wulff construction	76
5.3.3	Heterostructure interfaces	78
5.3.4	Workflows	83
5.4	Conclusions	85
6	Conclusions	86
	Bibliography	90

³To be published as 'Kiran Mathew, R. Sundararaman, D. Gunceler, T. A. Arias and R. G. Hennig, Self-consistent non-linear solvation model in plane-wave density-functional theory'

⁴To be published as 'Kiran Mathew, A. Singh, J. Gabriel, F. Tavazza, A. Davydov and R. G. Hennig, MPInterfaces: A Materials Project based python tool for a high throughput computational screening of interfacial systems'

LIST OF TABLES

2.1	Molecular solvation energies; VASP, JDFTx and experimental values. All energies are in eV	34
2.2	Energy barriers for the nucleophilic substitution S_N2 in vacuum and in water calculated with VASP, Gaussian09, and constrained <i>ab-initio</i> molecular dynamics.	38
4.1	Solvation energies of LiF (100) in units of eV per surface LiF unit	67
4.2	Surface energies of MgO and BeO slabs in units of eV/nm ² . . .	68
5.1	The lattice parameter, a (Å), of graphene and (111) surfaces of Pt, Cu, Au, Pt, Ni, Al and Ag is shown in the table. The lattice-mismatch between the primitive lattices of graphene and substrate, $\epsilon_{1:1}$ in (%), is compared with the lattice-mismatches obtained from <i>MPInterfaces</i> code, ϵ_{MP} (%). The supercells of substrate, S_{sub} , and graphene, S_{gr} , obtained from <i>MPInterfaces</i> are listed as well.	80

LIST OF FIGURES

1.1	Schematic diagram of electrode/electrolyte interface [1]. Double layer formation on a negatively charged electrode surface is depicted.	2
1.2	Schematic illustration of PbSe quantum dots when exposed to DMF. For an air-free sample, DMF treatment preferentially removes the ligands from the {100} facet, causing fusing along that direction and leading to square packed crystals. When particles are exposed to air, the {100} facets are oxidized preferentially. When the DMF further removes ligands, the oxide passivated particles agglomerate in an undirected, amorphous fashion [12].	4
1.3	Folding driven by local interactions, secondary structure formation precedes collapse [28].	4
1.4	Schematic diagram of surface/implicit solvent interface.	13
1.5	VASPsol logo.	15
2.1	Smooth variation of the relative permittivity ϵ from the vacuum value of one to the value of the solvent, e.g. 80 for water.	26
2.2	Solvation energy as function of the Gaussian ionic width for CO molecule for two different atomic separations, where the Gaussian width, σ , is specified in units of the grid size.	29
2.3	Comparison of solvation energies for different molecules in water calculated with VASP and JDFTx. The JDFTx calculations employed norm-conserving pseudopotentials and the VASP calculations ultrasoft pseudopotentials and the PAW method.	31
2.4	Experimental versus VASP calculated solvation energies for different molecules in water	33
2.5	Surface energies of the (111), (100), and (110) facets of Pt nanocrystals in different solvents.	36
2.6	Surface energies of the (100), (111), and (110) facets of PbS nanocrystals in different solvents.	37
2.7	Nucleophilic substitution S_N2 reaction of a chlorine ion with chloromethane.	38
3.1	Spatial decomposition of the solid/electrolyte system into the solute, interface, and electrolyte regions for a bcc Na(110) surface embedded in an electrolyte with relative permittivity $\epsilon_r = 78.4$ and monovalent cations and anions with concentration 1M. The solute is described by density-functional theory, the electrolyte by an implicit solvation model. The interface regions is formed self-consistently as a functional of the electronic density of the solute. All properties are shown as a percentage of their maximum absolute value.	43

3.2	Comparison between the computed and the experimental Potential of Zero Charge (PZC) with respect to the standard hydrogen electrode (SHE). The dashed line is a fit of $V^{\text{pred}} = V^{\text{exp}} + V_{\text{SHE}}^{\text{pred}}$ to determine the theoretical potential of the SHE.	49
3.3	Surface charge density of the Pt (111) surface as a function of applied electrostatic potential computed with the implicit electrolyte module, VASPsol. The slope of the curve determines the capacitance of the dielectric double layer.	51
3.4	Pt adatom(black) adsorbed on three different sites on the Pt 111 surface. Red, green and blue indicate top, second and third layers of Pt 111 respectively	52
3.5	Plot of voltage vs the adsorption energy	52
4.1	Plot of $ \vec{E} $, the magnitude of the electric field averaged over x-y plane, and the relative permittivity, averaged over x-y plane, for LiF 100 surface in Ethylene Carbonate solvent computed using the nonlinear solvation model.	56
4.2	Comparison between the computed, the experimental and jdftx solvation energies	65
5.1	(a) Top view of a rocksalt (100) surface of Lead Sulfide (PbS) denoted as PbS(100). High symmetry binding sites 1,2,3,4 on this facet are marked as orange, green, purple and red respectively. Lead (Pb) is indicated in blue and Sulfur (S) in yellow. Hydrazine ligand placed on (b) site 2, above an S atom on of PbS(100) bound through the Nitrogen (N - Green) atom on the ligand, (c) site 3 of PbS(100) referenced with adsorption distance bound through the Hydrogen (H - Grey) atom on the ligand, (d) site 4 of PbS(100) bound through the N atom on the ligand with a random rotation about cartesian axes, (e) higher coverage on site 1 above a Pb atom, binding through N atom, (f) a high coverage over site 4, binding through N atom. Notice the preservation of symmetry between the molecules to minimize the steric hindrance. Other entropic configurations can be included with manual manipulation of binding sites. We calculate the interfacial property of binding energy per ligand.	74
5.2	The shape of a PbS nanocrystal generated using the Wulff construction supported by <i>MPInterfaces</i> . The code snippet used for the creation of nanoparticle is provided. The surface energies are from the reference [68].	77
5.3	The algorithm of Zur <i>et al.</i> [107] for the epitaxial lattice-matching and symmetry-matching of any two surfaces for all rotations; within a given lattice mismatch and within a given surface area of the interface.	79

5.4 (a) Top view and (b) side view of 1:1 match between strained graphene and Ni(111) (or Cu(111)). (c) Top view and (d) side view of 2×2 graphene strained by $< 4\%$ to match the $\sqrt{3} \times \sqrt{3}$ supercells of Pt(111) (or Pd(111), Ag(111), Au(111) and Al(111)) surfaces. The primitive cell of graphene is shown with a yellow box, that of the substrates with a green box, and lattice-matched cells of graphene and substrates with a black box. Another configuration for (a) is shown in (e) top view and (f) side view, but with a different surface placement of the atoms at the interface. The substrate atoms beyond the third layer from the interface are hidden for clarity. 81

CHAPTER 1

INTRODUCTION

Multi-phase interfaces play a major role in the design and the understanding of modern microelectronic devices, energy storage devices and biological systems [49, 74, 16, 42]. The understanding of morphology and composition of the interfaces forms the key to the unfolding of new scientific phenomena that could eventually lead to the creation of better and efficient technological applications that have the potential of advancing the human civilization. Interfaces can be between solid and solid phases, solid and liquid phases or solid and gaseous phases. In comparison to the solid/solid and solid/gaseous interfaces, solid/liquid interfaces deserve special attention as they are more technologically important and pose a much tougher challenge to tackle computationally.

1.1 Importance of solid/liquid interfaces

Solid/liquid interfaces are ubiquitous in modern technological devices. From energy storage devices to the manufacturing of modern micro-electronics, all involve solid/liquid interfaces either in the working device or in the manufacturing process.

Consider the cases of electrochemical cells and batteries, where the electrode/electrolyte interface chemistry determines the operating voltage as well the stability of the device. Figure 1.1 shows the schematic diagram of electrode/electrolyte interface. Deposition on the electrodes and passivating layers formed on the surfaces of the electrodes are known to cause capacity fade in batteries [8], especially the lithium-ion cells [26]. In batteries utilizing lithium

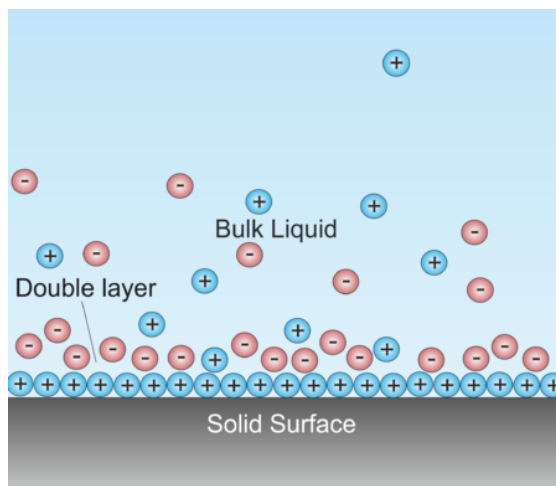


Figure 1.1: Schematic diagram of electrode/electrolyte interface [1]. Double layer formation on a negatively charged electrode surface is depicted.

metal, the formation of dendrite structures on lithium electrode could lead to short circuits, posing a serious safety concern [21, 65]. In order to improve the predictive capability of battery models, thus ultimately leading to less expensive and higher quality batteries, requires the quantification of the processes occurring at the interfaces. Typical battery performance standards such as energy density and cycle life require considerable improvements, while maintaining high environmental, safety and cost standards. Such progress will require significant advances in our understanding of electrode and electrolyte materials [8].

The synthesis of nanoparticle and their assembly is another research area where solid/liquid interfaces play a major role [11, 24, 12]. Like atoms or molecules, nanocrystals (NC) may be used as the building blocks for the assembly of novel solid-state materials. This opens up possibilities of fabricating new materials and devices with novel physical properties, as interactions between proximal NCs give rise to new collective phenomena [71]. Building upon the

understanding of the physical properties of individual NCs and the interacting between NCs, novel materials can be designed with properties that are controlled by the interplay of the individual NCs, their assembly, and the coupling by, *e.g.*, molecular ligands. Engineering the size and composition of the NCs will tune the properties of the individual NC building blocks. The electronic and optical properties of metals and semiconductors strongly depend on the crystalline size in the nanometer regime [16]. Selecting the length and chemical functionality of ligands can tune the synthesis of nanocrystals and the coupling between neighboring NCs. Nanoparticle size and shape depends largely on the ligands and the solvent medium in which they are dispersed in. Type and the number of ligands bound to the NC surfaces can become a deciding factor in NC self-assemblies [14]. The binding strength of various ligands on the NC facets as well as their coverage are significantly affected by the dispersive medium [24]. Figure 1.2 shows how solvent treatment can alter the self-assembly of PbSe NCs. Better understanding of the role of the interfaces between NCs, ligands, and solvents is needed to enable a rational design of these NC assemblies with specific properties.

Another area where solid/liquid interfaces play an important role are biological systems and their processes, such as protein folding and self assembly. In protein folding the interactions among the components in the amino acid sequence are the main determinants of the protein structure [29]. Figure 1.3 shows the schematic diagram of protein folding driven by local interactions. As with the NC/ligand interfaces, the dispersive medium plays a significant role in modifying the interactions within the protein chain as well as between protein chains [3].

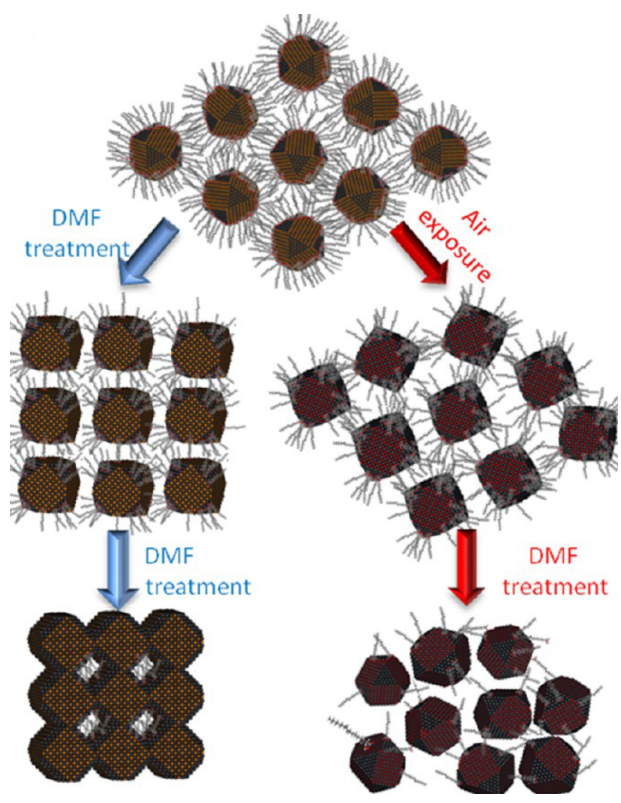


Figure 1.2: Schematic illustration of PbSe quantum dots when exposed to DMF. For an air-free sample, DMF treatment preferentially removes the ligands from the $\{100\}$ facet, causing fusing along that direction and leading to square packed crystals. When particles are exposed to air, the $\{100\}$ facets are oxidized preferentially. When the DMF further removes ligands, the oxide passivated particles agglomerate in an undirected, amorphous fashion [12].

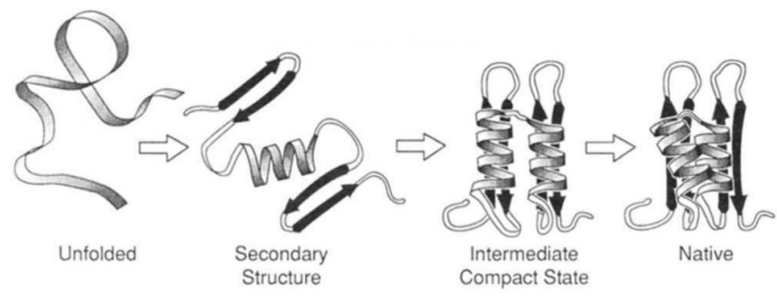


Figure 1.3: Folding driven by local interactions, secondary structure formation precedes collapse [28].

1.2 Computational approaches for multiscale modeling

Experimental methods such as X-ray spectroscopy, microscopy techniques such as atomic force microscopy (AFM), scanning tunneling microscope (STM), and transmission electron microscopy (TEM) *etc.* can provide a wealth of information on the electronic, optical and catalytic properties of a variety of systems. They can also shed light on the global as well as local structures of interfacial systems. But a complete and detailed understanding of solid/liquid interfaces by experimental techniques alone is difficult due to the heterogeneous and statistical nature of the interface, the importance of impurities in the system, and current limitations imposed by the expensive experimental techniques. Computational techniques can greatly supplement the knowledge gained from experimental observations and provide guidance towards newer exploratory directions.

Theoretical methods and simulations can provide complementary information such as energetic stability, the detailed electronic structure, energy barriers for reaction pathways, *etc.* However, most computational studies neglect the effect of solvents and electrolyte for solid/liquid interfaces or are limited by the time-consuming generation of structures for solid/solid interfaces. Also when it comes to computational modeling different mathematical models need to be considered to describe various phenomena occurring over a range of length and time scales.

Electronic structure theory that describes the system at an electronic level constitute the lower end of the length and time scale. In principle one could use the electronic structure theory to describe any arbitrary system, but the amount

of degrees of freedom involved in solving the system at that level makes the treatment not amenable to a numerical solution even with the state of the art computational resources. Atomistic models such as Molecular dynamics simulations are employed successfully to describe systems at an atomic level without accounting for the electronic degrees of freedom. Even higher level of description is utilized in the continuum models where both electronic as well as atomic degrees of freedom are averaged out.

Often different models need to be combined to ensure an efficient and accurate theoretical framework to describe the system under consideration properly. In this thesis we develop multi-scale methods and algorithms for the accurate description of solid/liquid interfaces and the efficient high-throughput calculation of materials interfaces. The description of solid/liquid interfaces are based on concurrent multi-scale approach that couple accurate density-functional theory for the solid with efficient continuum models for the liquid. In the following we provide brief introduction to electronic structure methods with focus on density-functional theory, continuum solvation models, and high-throughput frameworks for materials calculations.

1.2.1 Electronic structure methods

Within the Born-Oppenheimer approximation the electronic structure problem is finding the ground state energy of non-relativistic electrons for arbitrary nuclear positions [20]. Once the solution is known, many properties like bond energies and bond lengths of molecules and lattice structures and the band structure of solids can be predicted [33]. The Hamiltonian for N electrons is given

by [54]

$$\hat{H} = \hat{T} + \hat{V}_{ee} + \hat{V}_{ext}, \quad (1.1)$$

where the kinetic energy operator, \hat{T} , is given by

$$\hat{T} = -\frac{1}{2} \sum_1^N \nabla_j^2, \quad (1.2)$$

the electron-electron repulsion operator is given by

$$\hat{V}_{ee} = \frac{1}{2} \sum_{i \neq j} \frac{1}{|r_i - r_j|}, \quad (1.3)$$

and the external potential describing the nuclei-electron interaction is given by

$$\hat{V}_{ext} = \frac{1}{2} \sum_I \sum_i \frac{Z_I}{|R_I - r_i|}, \quad (1.4)$$

The ground state energy satisfies the variational principle:

$$E = \min_{\Psi} \langle \Psi | \hat{H} | \Psi \rangle \quad (1.5)$$

where the minimization is over all anti symmetric N -particle wavefunctions.

Solving the aforementioned full N -electron Schrödinger's equation is impossible even with the state of the art computational resources. Reasonable approximations need to be made to solve the problem without losing the accuracy. Simplest of such approximations is the Hartree approximation where the wavefunction is given by the non-interacting single particle orbitals [53]

$$\Psi = \phi_1(r_1)\phi_1(r_2)\dots\phi_N(r_N), \quad (1.6)$$

where $\phi_i(r_i)$ is the single particle orbital. Within this approximation the energy term corresponding to the electron-electron repulsion is given by

$$E_{ee} = \int d^3r \int d^3r' \frac{\sum_i |\phi_i(r')|^2 \sum_i |\phi_i(r)|^2}{2|r - r'|} \quad (1.7)$$

The above energy term is called the Hartree energy. Its a mean field term that accounts for the electronic repulsion in an average sense. The Hartree approximation fails to account for the anti-symmetric property of the wavefunction and the electron-electron correlations. Next in line of several approximations is the Hartree-Fock approximation that approximated Ψ by a single Slater determinant of single particle orbitals [53].

$$\Psi = \sum_p (-1)^p \Pi_i \phi_i(r_p), \quad (1.8)$$

where p is a permutation. In addition to the mean field term in the Hartree approximation, Hartree-Fock theory contributes an additional term called the exchange term that results from the anti-symmetric nature of the wavefunction [15].

$$E_{exchange} = - \int d^3 r \int d^3 r' \frac{\phi_i(r)\phi_j^*(r)\phi_i^*(r')\phi_j(r')}{2|r-r'|} \quad (1.9)$$

Although the Hartree-Fock approximation was able to capture most of the physics but it still failed to account for the electron correlation effects. Other approaches such as the configuration interactions[87], couple cluster [82] and the Moller-Plesset perturbation [81] theory were developed to accurately account for the electron correlation effects. These accurate methods demand more complicated calculations and the computational resource requirement increases exponentially with the system size. There needs to be a compromise between the required accuracy and the ease of solving the problem. The density functional theory approach provides such an efficient alternative approach.

Density functional theory

In density functional theory (DFT) the ground state energy is written in terms of the electronic charge density, $n(r)$, instead of the wavefunction Ψ , where the charge density is given by

$$n(r) = |\Psi|^2. \quad (1.10)$$

The first such DFT formulation was by Thomas and Fermi [61]. In that formulation, the kinetic energy density at any point is approximated by that of uniform electron gas of non-interacting electrons of density $n(r)$ i.e

$$\hat{T}_{TF} = \frac{3(3\pi^2)^{2/3}}{10} \int n(r)^{5/3} d^3r. \quad (1.11)$$

The electron-electron repulsion term is given by the Hartree energy term mentioned before

$$E_H = \frac{1}{2} \int d^3r \int d^3r' \frac{n(r)n(r')}{|r - r'|}. \quad (1.12)$$

The nuclei-electron interaction term, labeled the external energy contribution, is given by

$$E_{ext} = \int d^3r V_{ext}(r)n(r). \quad (1.13)$$

Thus the net system energy as a functional of the charge density becomes

$$E[n(r)] = T_{TF}[n(r)] + E_H[n(r)] + E_{ion}[n(r)]. \quad (1.14)$$

Minimizing the above energy functional yields the ground state.

Though the Thomas-Fermi approximation is able to compute the energies correctly for many systems, the approximation is very ad hoc and no rigorous proof for the existence of a charge density dependent ground state is provided. In 1964, the theory proposed by Hohenberg-Kohn [45] changed the electronic structure landscape significantly by providing a rigorous proof for DFT. The

Hohenberg-Kohn theorem that forms the central tenet of DFT states the following:

- There exists a functional $F[n]$ of the electron density such that the ground state energy and the density for N -electron system in the presence of the external potential V_{ext} is

$$E_0 = \min_n \{F[n(r)] + \int d^3r V_{ext}(r)n(r)\}. \quad (1.15)$$

The minimum is taken over all positive n such that $\int d^3r n(r) = N$ where N is the number of electrons in the system. $F[n]$ is the the universal function independent of V_{ext}

- The external potential V_{ext} and hence the Hamiltonian \hat{H} are determined to within an additive constant by the charge density, $n(r)$.

The problem is to find or approximate the functional $F[n(r)]$. The scheme introduced by Kohn and Sham in 1965 [101] calculates most parts of the universal functional exactly. The scheme computes the kinetic energy and the Hartree energy term exactly using a anti symmetric non-interacting wavefunction such that wavefunction produces the same density $n(r)$. Thus the universal functional is given by

$$F[n] = T[n] + E_{hartree}[n] + E_{xc}[n]. \quad (1.16)$$

The last term E_{xc} , called the exchange-correlation energy accounts for the exchange and the correlation contribution to the energy that were missed out in the non-interacting approximation. Minimizing the energy functional under the Kohn-Sham scheme yields the Schrödinger equation with the Kohn-Sham Hamiltonian H_{KS} :

$$\hat{H}_{KS}\phi_j = \epsilon_j\phi_j, \quad (1.17)$$

where ϕ_j and ϵ_j are the Kohn-Sham Orbitals and eigenvalues respectively and the Kohn-Sham Hamiltonian is given by

$$H_{KS} = -\frac{1}{2}\nabla^2 + \hat{V}_{KS}, \quad (1.18)$$

where \hat{V}_{KS} is the Kohn-Sham potential:

$$\hat{V}_{KS} = \hat{V}_H + \hat{V}_{ext} + \hat{V}_{XC}, \quad (1.19)$$

where \hat{V}_H is the Hartree potential given by

$$\hat{V}_H(r) = \int d^3r' \frac{n(r')}{|r - r'|} \quad (1.20)$$

and \hat{V}_{XC} is the exchange-correlation potential:

$$\hat{V}_{XC} = \frac{\delta E_{XC}}{\delta n(r)}. \quad (1.21)$$

The Kohn-Sham scheme is exact but in practice approximations need to be made for the exchange-correlation energy term. The approximation that one makes for the exchange correlation energy term is the primary source of different flavors of DFT that are in existence today. Most widely used approximations are: the local density approximation (LDA) [15] and the generalized gradient approximation (GGA) [15]. In LDA the the exchange-correlation energy density corresponds to that of uniform electronic gas of density n whereas in the case of GGA the energy density is a functional of the charge density and its gradient, $|\vec{\nabla}n|$:

$$E_{XC}^{LDA} = \int d^3r \epsilon(n) \quad (1.22)$$

$$E_{XC}^{GGA} = \int d^3r \epsilon(n, |\vec{\nabla}n|). \quad (1.23)$$

There are numerous implementations of Kohn-Sham DFT. They vary mostly in the choice of basis functions used in expanding the single particle Kohn-Sham

orbitals. For periodic systems, the choice of plane waves prove to be the best choice as it enables the use of the efficient Fast Fourier Transforms (FFT). The implementations of the solvation models described in this work are done in the widely used plane-wave DFT code VASP [56].

Coupling continuum solvent models with density functional theory

DFT provides a reliable and efficient means to study the electronic structure of crystal systems. It has been applied successfully towards the design and understanding of a wide variety of novel solid systems and surfaces. But DFT treatment of liquids present an enormous challenge due to its lack of structure.

Including the solvent effects in DFT calculation by adding explicit solvent molecules is the most straight forward thing to do as it involves only specifying the atomic positions of the solvent molecules, the same way one would go about with crystal systems. There in lies the problem because unlike crystal structures liquids lack a defined structure and the computation of liquid properties require statistical averaging over a large number of ensembles. This means a larger simulation box to incorporate the large number of solvent molecules to capture their complete effect on the surface and also a longer simulation time to facilitate the required thermodynamic sampling. Even though DFT significantly reduces the degrees of freedom that need to be solved in comparison to the N -electron wavefunction, the calculations could still be expensive as the system scales as N^3 where N is the number of electrons in the simulation box. Thus a very accurate DFT calculation with explicit solvent becomes prohibitively expensive even for the modern state of the art machines.

Instead of treating the solvents explicitly, it is possible to account for their effects on the solute in an implicit manner. In this approach the solvents are characterized by their equilibrium properties such as the relative permittivity, density, permanent dipole moment of the solvent molecule *etc*, instead of as a collection of molecules. Figure 1.4 shows the schematic of formic acid molecule adsorbed on Pt surface embedded in an implicit solvent medium. Most commonly employed implicit solvent models are the polarizable continuum models (PCM) [97]. In PCM the solute system is assumed to be embedded in a dielectric cavity and the interactions between the solute and the solvent are entirely electrostatic in nature. Further corrections can be made by adding energy terms that account for the dispersion and hydrophobic effects between the solute and the solvent. As with the Thomas-Fermi model in DFT, the PCM models are ad hoc and not rigorous.

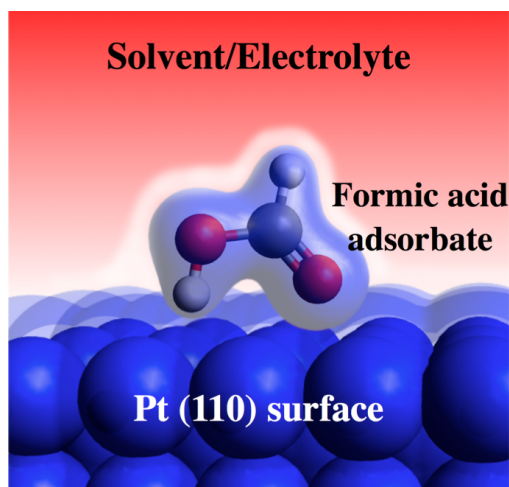


Figure 1.4: Schematic diagram of surface/implicit solvent interface.

Work by Arias et al. [79], the joint density functional theory (JDFT) puts the solvent effects into a rigorous DFT framework. Various PCM models can be then seen as the various approximations to the JDFT. JDFT introduces a variational theorem that allows an exact description of the solute/solvent systems in

terms of electron densities for the solute part of the system and in terms of fluid nuclear densities for the solvent. Petrosyan et al. [78] shows that the equilibrium free energy of a solvated electronic system minimizes

$$E_0 = \min_{n, \{N_\alpha\}} [F_{JDFT}[n, \{N_\alpha\}] + \int dr V_{ext} n(r) + \sum_\alpha \int dr V_\alpha N_\alpha(r)], \quad (1.24)$$

where F_{JDFT} is a universal functional of the solute electronic density and the solvent nuclear densities alone. Similar to the universal functional in the Hohenberg-Kohn theorem the JDFT universal functional can be decomposed exactly as

$$F_{JDFT}[n, \{N_\alpha\}] = F_{HK}[n] + E_{liquid}[\{N_\alpha\}] + \Delta E[n, \{N_\alpha\}], \quad (1.25)$$

where F_{HK} is the universal functional from the Hohenberg-Kohn theorem, E_{liquid} is the free energy functional of the liquid and the last term is the coupling term that accounts for the interaction between the solute and solvent systems. Different solvent models come about as a result of the approximations one make for the JDFT universal functional, F_{JDFT} . The following chapters in the thesis describe PCM like models that are cast into the rigorous framework of the joint density functional theory.

In this thesis I describe the self-consistent implementation of a set of solvent models into the widely used plane-wave DFT code VASP [56]. The open-source implementation, VASPsol [68], is freely available and is part of the official VASP release from versions $\geq 5.4.1$. The VASPsol logo is depicted in Figure 1.5.

Chapter 2 describes the linear solvation model for a dielectric continuum and its self-consistent implementation in VASP. Chapter 3 describes how we extend the model to include the description of the shielding through mobile ions in electrolyte solutions and its self-consistent implementation in VASP. Chapter 4 furthermore expands the solvation models to include a description of dielectric

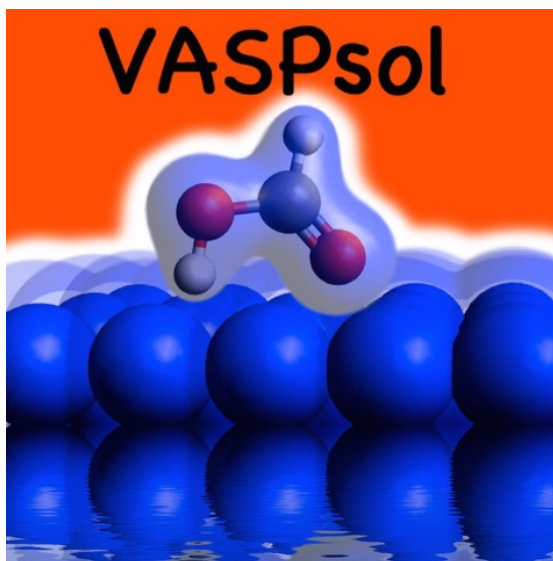


Figure 1.5: VASPsol logo.

saturation at high electric fields as can occur near electrode interfaces and the effect of finite size of the ions. In each chapter, following a brief review of the energy functionals describing the solvent interactions, we derive the modified Kohn-Sham potential that casts the model into a self-consistency framework so that it can be integrated into the self-consistent plane wave DFT code VASP. The implementation details are also discussed in each chapter.

1.2.2 High-throughput framework for screening interfaces

The above described methodologies coupled with numerous computational tools that already exist provide an excellent infrastructure for the analysis of various interfacial systems. The software tools that enable methodologies like molecular dynamics (MD), kinetic monte carlo (KMC) and Finite Element Methods (FEM) enable one to study systems at various length scales ranging from nano to macro. Bridging the gap between ab-intio studies and a macroscopic

analysis of systems require appropriate software frameworks that can couple with the existing tools and integrate them into one common framework that can be employed to do a full scale analysis of the system under consideration. Advancement in modern computing enables today's computational scientist to pursue such a more balanced and holistic approach to the discovery of advanced materials. Acceleration of the discovery of novel materials requires the development of framework/management systems can efficiently leverage the available tools and computational resources.

Chapter 5 describes the development and implementation of such a framework. The open-source framework written in python programming language enables screening of interfacial systems in a high throughput fashion. The framework extends the already existing efficient resources that are part of the Materials Project [73], which is part of the materials genome initiative announce couple of years ago to fast forward the materials research. The frameworks capabilities can be the grouped into three categories:

1. Generate structures of arbitrary interfacial systems such as solid/implicit liquid, nanocrystal/ligand and heterostructure interfaces. The generated structures can be formatted to conform with the computational tool being used
2. Generate input files for various softwares that implement molecular dynamics (MD) and DFT methodologies.
3. Enable creation of workflows that describe the steps in the analysis with support for the mixing of various software tools.
4. Provide a unified framework for the workflow execution on all available diverse computing resources.

CHAPTER 2
SELF-CONSISTENT LINEAR SOLVATION MODEL IN PLANE-WAVE
DENSITY-FUNCTIONAL THEORY ¹

2.1 Abstract

Solid-liquid interfaces are at the heart of many modern-day technologies and provide a challenge to many materials simulation methods. A realistic first-principles computational study of such systems entails the inclusion of solvent effects. In this work we implement an implicit solvation model that has a firm theoretical foundation into the widely used density-functional code VASP. The implicit solvation model follows the framework of joint density functional theory. We describe the framework, our algorithm and implementation, and benchmarks for small molecular systems. We apply the solvation model to study the surface energies of different facets of semiconducting and metallic nanocrystals and the S_N2 reaction pathway. We find that solvation reduces the surface energies of the nanocrystals, especially for the semiconducting ones and increases the energy barrier of the S_N2 reaction.

2.2 Introduction

Recently, scientists have determined that the understanding of nanoparticle synthesis and electrochemical interfaces is crucial to designing novel materials for energy technology and improving the performance characteristics of batter-

¹Published as 'Kiran Mathew, R. Sundararaman, K. Letchworth-Weaver, T. A. Arias, and R. G. Hennig, *J. Chem. Phys.*, 140(8):084106, 2014'

ies and catalysts. [11, 14, 43, 102] The physics of solid-liquid interfaces plays a major role in the synthesis of nanoparticles, chemical reactions at electrode surfaces, [63] and in many other phenomena important to energy applications. The thermodynamics and kinetics of nanoparticle interfaces determine the particle morphologies and surface states, which in turn affect the self-assembly as well as optical and electronic properties of these materials. [24, 22, 52]

A comprehensive understanding of nanoparticle synthesis and electrochemical interfaces via experiments presents a challenge due to the heterogeneity of the interface and the complexities of the solid and liquid materials involved. [70] Computational studies provide an alternative method to improve our fundamental understanding of solid/liquid interfaces and to predict properties of novel materials interfaces. [14, 60, 88, 31]

There are two main ways to achieve a computational treatment of solid/liquid interfaces. If a complete *ab-initio* treatment of the solute/solvent system is desired, all solvent molecules must be considered explicitly. Thus, to reach the equilibrium state we need to relax the electronic and ionic degrees of freedom of both the solute and the solvent molecules. This treatment is quite expensive, as the number of solvent molecules in the system required to capture the essential equilibrium properties is huge and because of the statistical averaging required for the solvent molecules.

An alternative approach is to treat the solute quantum-mechanically and to treat the solvent as a continuum, which means that the solute is immersed in a bath of solvent and the average over the solvent degrees of freedom becomes implicit in the properties of the solvent bath. Implicit solvation models for plane wave density-functional theory (DFT) codes were pioneered by Fattbert and

Gygi, [31] independently developed and placed into the rigorous framework of joint density functional theory (JDFT) by Arias *et al.*, [79] and extended by Marzari *et al.* to include a model for cavitation and dispersion. [5] These methods provide a much more computationally tractable way to vary the electronic and the geometric degrees of freedom of the solute so that the ground state of the combined solute/solvent system conforms with the equilibrium properties of the solvent bath. Since the solute electronic structure is still being treated quantum-mechanically, this approach can be quite accurate assuming all interactions between the solute and the solvent are considered in proper detail.

For polar or ionic solute systems in contact with polar fluids, the electrostatic interaction between the solute and the solvent is the most significant solvation effect. For nonpolar solutes and solvents, the van der Waals interaction can dominate over electrostatics. For large molecules, the energy required to form a cavity in the solvent is the most important contribution to the solvation energy. Thus, any solvation theory which can be generally applicable to nanoparticles, molecules, and surfaces must consider all of these effects. In this work, we review an implicit solvation model which places a quantum-mechanical solute in a cavity surrounded by a continuum dielectric description of the solvent. Describing the dielectric response as a functional of the solute electronic charge density leads to a self-consistent determination of the cavity by considering the polarization of the solvent by the electronic structure of solute, the effects of cavitation and dispersion, and the corresponding response of the solute system to the presence of the solvent. This implicit solvation model provides a computationally efficient and accurate technique for understanding solute/solvent interfaces.

Following the approach of Refs. [[60]] and [[79]], we briefly review the theoretical underpinnings and framework of these implicit solvation models in Sec. 2.3. We then describe in Sec. 2.4 the implementation of an implicit solvation model derived from joint density functional theory [60, 79, 41] in VASP, a widely used and multi-featured plane-wave DFT code. Though this model was previously implemented in the open source codes DFT++ [47] and JDFTx, [95] implementation in VASP places this theory into the self-consistent field framework for the first time. Due to the plane-wave basis, this implementation is more scalable for large periodic systems than solvation models which employ Gaussian type orbitals. Additional advantages of this new implementation include higher performance, better MPI parallel scaling, and the interoperability with an extensive library of standardized ultrasoft pseudopotential and projector-augmented wave potentials. In Sec. 2.5 we benchmark the accuracy of this implementation by calculating molecular solvation energies, and comparing against both experimental and JDFTx-calculated values. Finally, in Section 2.6 we apply the model to metal and semiconductor nanocrystal interfaces and reaction pathways. We find that the implicit solvation model that we have implemented into VASP provides an efficient and accurate approach to determine solvation energies of molecular and extended systems. Also, the solvation modifications are freely available as a patch to the original VASP source code. [66]

2.3 Theoretical framework of implicit solvation model

Following Refs. [[79]] and [[78]], the free energy, A , of the combined solute/solvent system can be written as a sum of two terms, a universal functional F of the total electron density and the thermodynamically averaged atomic densities of

the solvent species, and a term describing the electrostatic energy contribution

$$A = F[n_{\text{tot}}, \{N_i(\vec{r})\}] + \int d^3r V_{\text{ext}}(\vec{r}) \left(\sum_i Z_i N_i(\vec{r}) - n_{\text{tot}}(\vec{r}) \right). \quad (2.1)$$

Here $n_{\text{tot}}(\vec{r})$ is the total electron density, which is the sum of the electron density of the solute and the solvent, i.e. $n_{\text{tot}}(\vec{r}) = n_{\text{solute}}(\vec{r}) + n_{\text{solvent}}(\vec{r})$. $N_i(\vec{r})$ are the thermodynamically averaged atomic densities associated with the chemical species i in the solvent, $V_{\text{ext}}(\vec{r})$ is the external potential due to the solute nuclei and F is a universal functional. The functional F is universal in the sense that it depends only on the electron density, the solvent atomic densities, and thermodynamic parameters such as temperature and pressure. A detailed discussion of the theoretical consequences can be found in Ref. [[96]].

Next we use the variational principle for the thermodynamic free energy of the electron-nuclear system in a fixed external electrostatic potential $V_{\text{ext}}(\vec{r})$ to determine the ground-state free energy of the system

$$A_0 = \min_{n_{\text{tot}}, \{N_i(\vec{r})\}} \left\{ F[n_{\text{tot}}, \{N_i(\vec{r})\}] + \int d^3r V_{\text{ext}}(\vec{r}) \left(\sum_i Z_i N_i(\vec{r}) - n_{\text{tot}}(\vec{r}) \right) \right\}. \quad (2.2)$$

Although the above formalism provides an exact DFT treatment of the combined solute/solvent system, it is difficult to solve in practice due to the minimization involved over the immense number of solvent degrees of freedom. In order to make it amenable to a computational treatment, the free energy is first minimized over the solvent electron density and then over the solute electron density to determine the ground state free energy. [79]

Minimizing Eq. (2.1) with respect to the solvent electron density n_{solvent} , we

obtain

$$\begin{aligned}\tilde{A} &= G[n_{\text{solute}}(\vec{r}), \{N_i(\vec{r})\}, V_{\text{ext}}(\vec{r})] \\ &\quad - \int d^3r V_{\text{ext}}(\vec{r})n_{\text{solute}}(\vec{r}),\end{aligned}\quad (2.3)$$

where

$$\begin{aligned}G[n_{\text{solute}}(\vec{r}), \{N_i(\vec{r})\}, V_{\text{ext}}(\vec{r})] &= \min_{n_{\text{solv}}} \left\{ F[n_{\text{tot}}, \{N_i(\vec{r})\}] \right. \\ &\quad \left. - \int d^3r V_{\text{ext}}(\vec{r}) \left(\sum_i Z_i N_i(\vec{r}) - n_{\text{solv}}(\vec{r}) \right) \right\}.\end{aligned}\quad (2.4)$$

G is a universal functional of the electron density of the solute $n_{\text{solute}}(\vec{r})$, the average atomic densities of the various species in the solvent $\{N_i(\vec{r})\}$, and the external potential of the solute nuclei $V_{\text{ext}}(\vec{r})$. The functional G can be separated as following

$$\begin{aligned}G[n_{\text{solute}}(\vec{r}), \{N_i(\vec{r})\}, V_{\text{ext}}(\vec{r})] &= A_{\text{KS}}[n_{\text{solute}}(\vec{r}), V_{\text{ext}}(\vec{r})] + \\ &\quad + A_{\text{diel}}[n_{\text{solute}}(\vec{r}), \{N_i(\vec{r})\}, V_{\text{ext}}(\vec{r})],\end{aligned}\quad (2.5)$$

where A_{KS} is the usual Kohn-Sham density functional for the solute and A_{diel} is the term that encapsulates all the interactions of the solute with the solvent and the internal energy of the solvent. To further simplify the expression, the functional A_{diel} is minimized with respect to the average atomic densities of the solvent, $N_i(\vec{r})$,

$$\begin{aligned}\tilde{A}_{\text{diel}}[n_{\text{solute}}(\vec{r}), V_{\text{ext}}(\vec{r})] &= \\ &\quad \min_{\{N_i(\vec{r})\}} A_{\text{diel}}[n_{\text{solute}}(\vec{r}), \{N_i(\vec{r})\}, V_{\text{ext}}(\vec{r})].\end{aligned}\quad (2.6)$$

Combining Eqs. (2.2) to (2.6) leads to the ground state free energy of the solute/-solvent system,

$$\begin{aligned}A_0 &= \min_{n_{\text{solute}}(\vec{r})} \left\{ A_{\text{KS}}[n_{\text{solute}}(\vec{r}), V_{\text{ext}}(\vec{r})] \right. \\ &\quad \left. - \int d^3r V_{\text{ext}}(\vec{r})n_{\text{solute}}(\vec{r}) + \tilde{A}_{\text{diel}}[n_{\text{solute}}(\vec{r}), V_{\text{ext}}(\vec{r})] \right\}.\end{aligned}\quad (2.7)$$

Importantly, this minimization procedure leads to a free energy of the combined solute-solvent system written as a functional of only the electron density of the solute, $n_{\text{solute}}(\vec{r})$, and the external potential of the solute nuclei, $V_{\text{ext}}(\vec{r})$, properties determined solely by the solute. All the solvent effects are contained in the functional \tilde{A}_{diel} , which is obtained by the minimization over the solvent electron density and the thermodynamically average atomic densities of the solvent. Thus, the functional \tilde{A}_{diel} describes a continuum model for the solvent, which has an equilibrium structure fully determined by the properties of the solute, upon the solute electronic structure. The minimization of the functionals in Eq. (2.7) with respect to the solute degrees of freedom leads to the ground state free energy of the joint system. Up to this point, the theory is exact, although the exact form of \tilde{A}_{diel} is unknown. Approximations must be made to the functional \tilde{A}_{diel} for practical calculations.

As a first approximation, we consider the electrostatic interaction between the solute and the solvent, which affects the equilibrium polarization of the solvent dipoles. Assuming that the solvent polarization depends linearly on the electric field for the range of fields encountered in the vicinity of the solute, the solvent polarization can be described by the local relative permittivity of the solvent, $\epsilon(\vec{r})$. We must then include in the functional \tilde{A}_{diel} a term to account for the electrostatic interaction between the solute electronic structure and the corresponding bound charge distribution induced in the solvent. [31, 79]

However, an electrostatic-only approach is insufficient to describe solvation of molecules and nanoparticles, where cavitation and dispersion may play a significant role. Since the non-electrostatic effects are concentrated in the first solvation shell, to describe these effects, [25] we adopt a version of the empirical

model proposed by Marzari *et al.*, [5] and placed into the joint density-functional theory framework by Arias *et al.* [41] that describes the corrections as an interface term that is proportional to the solvent-accessible area. Thus, we also include in \tilde{A}_{diel} an additional term to describe the free energy contributions of cavitation and dispersion,

$$A_{\text{cav}} = \tau \int d^3r |\nabla S|, \quad (2.8)$$

where τ is the effective surface tension parameter, which describes the cavitation, dispersion and the repulsion interaction between the solute and the solvent that are not captured by the electrostatic terms alone and $S(\vec{r})$ is the cavity shape function described below.

Decoupling the electrostatic term from the Kohn-Sham functional A_{KS} and combining it with the interaction term and the cavitation term, we obtain

$$\begin{aligned} A[n_{\text{solute}}(\vec{r}), \phi(\vec{r})] = & A_{\text{TXC}}[n_{\text{solute}}(\vec{r})] \\ & + \int d^3r \phi(\vec{r}) (N_{\text{solute}}(\vec{r}) - n_{\text{solute}}(\vec{r})) \\ & - \int d^3r \epsilon(\vec{r}) \frac{|\nabla \phi|^2}{8\pi} \\ & + A_{\text{cav}}, \end{aligned} \quad (2.9)$$

where A_{TXC} is the free energy density functional describing the kinetic and exchange-correlation energy of the solute and $N_{\text{solute}}(\vec{r})$ is the solute nuclear charge density.

We make an important distinction between the potentials $\phi(\vec{r})$ and $V_{\text{ext}}(\vec{r})$. $\phi(\vec{r})$ is the combined electrostatic potential due to the electronic ($n_{\text{solute}}(\vec{r})$) and nuclear ($N_{\text{solute}}(\vec{r})$) charges of the solute system in a polarizable medium. $V_{\text{ext}}(\vec{r})$ is the potential due to the nuclei in the solute, and is usually described by pseu-

dopotentials or the projector-augmented wave method. Outside a specified cut-off radius it has the form $\frac{Z_{\text{eff}}}{r}$, where Z_{eff} is the effective charge of the respective atom. Since the solvent described by $\epsilon(\vec{r})$ does not penetrate the core region of the pseudopotentials, we can approximate the contribution of the nuclear charges to the combined electrostatic potential $\phi(\vec{r})$ of the solute by a sum over terms of the form $\frac{Z_{\text{eff}}}{r}$.

So far, we have described a solute system surrounded by a dielectric medium quantified by the relative permittivity of the solvent system, $\epsilon(\vec{r})$. However, we must also determine the form of the dielectric cavity formed in the solvent by the solute. Implicit solvation models often differ in their approximations for this cavity. A common way to construct the cavity is to place spheres around the solute atoms and then take the union of these overlapping spheres. [97] Inside the so-formed cavity the relative permittivity is assumed to be that of vacuum, outside it takes the value of the solvent, and the induced charges are placed on the surface of this cavity. One might also assume a diffuse dielectric cavity such that the relative permittivity changes continuously.

In this work, we assume a diffuse dielectric cavity that is a local functional of the electronic charge density of the solute, i.e for the relative permittivity $\epsilon(\vec{r}) = \epsilon(n_{\text{solute}}(\vec{r}))$. This assumption leads to a diffuse cavity that is implicitly determined by the electronic structure of the solute. The smooth transition into the cavity also ensures that the derivatives of the energy functional are continuous, thereby simplifying the implementation of the geometric optimization of the solute system. We assume the following functional dependence [79] of the relative permittivity of the solvent on the solute electronic charge density

$$\epsilon(n_{\text{solute}}(\vec{r})) = 1 + (\epsilon_{\text{b}} - 1)S(n_{\text{solute}}(\vec{r})), \quad (2.10)$$

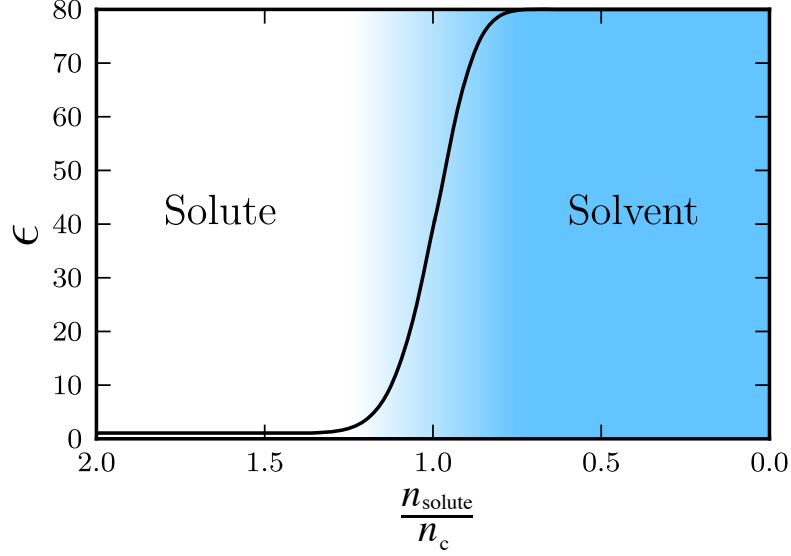


Figure 2.1: Smooth variation of the relative permittivity ϵ from the vacuum value of one to the value of the solvent, e.g. 80 for water.

where ϵ_b is the relative permittivity of the bulk solvent and $S(n_{\text{solute}}(\vec{r}))$ is the cavity shape function, given by

$$S(n_{\text{solute}}(\vec{r})) = \frac{1}{2} \operatorname{erfc} \left\{ \frac{\log(n_{\text{solute}}/n_c)}{\sigma \sqrt{2}} \right\}. \quad (2.11)$$

The parameter n_c determines at what value of the electron density the dielectric cavity forms, and σ is the parameter that determines the width of the diffuse cavity. The choice of the logarithm in the shape function is to obtain a numerically resolvable smoothly varying function for the usually exponentially decaying charge density. [79] Figure 2.1 illustrates the dependence of the permittivity on the solute electronic charge density. The above functional form of the relative permittivity ensures that the value of the relative permittivity varies smoothly from one in the bulk of the solute to ϵ_b in the bulk of the solvent and that for $\epsilon_b \rightarrow 1$, the free energy reduces to the vacuum value. This gradual variation emulates the first solvation shell effects, i.e the value of the relative permittivity of the solvent close to the solute is smaller than the equilibrium bulk value

due to the higher electric field near the solute surface, a phenomenon known as dielectric saturation.

As shown by Refs. [[60]] and [[79]], the functional in Eq. (2.9) can be optimized by first minimizing with respect to the electrostatic potential, $\phi(\vec{r})$, and then with respect to the solute electronic charge density, $n_{\text{solute}}(\vec{r})$. Minimization with respect to $\phi(\vec{r})$ leads to a generalized Poisson equation [31]

$$\begin{aligned} \nabla \cdot [\epsilon(n_{\text{solute}}(\vec{r}))\nabla\phi] = \\ - 4\pi \{N_{\text{solute}}(\vec{r}) - n_{\text{solute}}(\vec{r})\}, \end{aligned} \quad (2.12)$$

where $N_{\text{solute}}(\vec{r})$ consists of the effective core charges approximated by Gaussians as described below and $n_{\text{solute}}(\vec{r})$ is the valence electronic charge density. Minimization of Eq. (2.9) with respect to the electronic charge density, $n_{\text{solute}}(\vec{r})$, yields the typical Kohn-Sham Hamiltonian with the following additional terms in the local part of the potential

$$V_{\text{solv}} = \frac{d\epsilon(n_{\text{solute}}(\vec{r}))}{dn_{\text{solute}}(\vec{r})} \frac{|\nabla\phi|^2}{8\pi} + \tau \frac{d|\nabla S|}{dn_{\text{solute}}(\vec{r})}. \quad (2.13)$$

Corrections to the Hellman-Feynman force terms should also be made due the modifications of the Kohn-Sham potential. The force corrections consist of two terms,

$$\int \Delta\phi \frac{dN_{\text{solute}}}{dR_I} d^3r + \int V_{\text{solv}} \frac{dn_{\text{solute}}}{dR_I} d^3r. \quad (2.14)$$

The first term is due to the change in the electrostatic potential $\Delta\phi$, which is the difference between the solution to Eq. (2.12) and the electrostatic potential when the relative permittivity is one. The second term is due to the augmentation of the electronic charge density with the pseudo-charge density at the atom locations to prevent the fluid from entering in the core region, as described in the following section.

2.4 Implementation of implicit solvation model

The implicit solvation model reviewed above has been implemented into the Vienna Ab-initio Software Package (VASP), [56] a widely-used plane-wave DFT code. Combined with VASP’s parallel scalability to large system sizes and the availability of established and tested libraries of ultrasoft pseudo-potentials (USPP) [100, 57] and projector-augmented wave (PAW) potentials, [18] the MPI compatible implementation extends the capabilities of the software to study large solvated metallic and semiconducting systems in an efficient manner.

The VASP code solves the Kohn-Sham equations through self-consistent iterations to find the electronic ground state. To include the description of the solvent effects, we modify the local potential of the Kohn-Sham Hamiltonian and the expression for the total free energy. The solution to the generalized Poisson equation, given by Eq. (2.12), must become part of the self consistent loop as the valence charge density changes in each self-consistent iteration.

The generalized Poisson equation is solved in each electronic step to obtain the electrostatic potential of the combined solute electronic charge density and ionic charge density in the polarizable medium that describes the solvent. Since VASP is a plane-wave DFT code, we take advantage of fast Fourier transformation (FFT) methods and approximate the nuclear point charges by Gaussians of finite width, [79]

$$N_{\text{solute}}(\vec{r}) = \sum_I \frac{Z_I}{(2\pi\sigma)^{3/2}} \exp\left(-\frac{(\vec{r} - \vec{R}_I)^2}{2\sigma^2}\right), \quad (2.15)$$

where σ is the width of the Gaussian, \vec{R}_I and Z_I are the positions and charges, respectively, of the nuclear species I in the solute. As long as the width, σ is sufficiently small such that the Gaussians do not interfere with the solvent, the

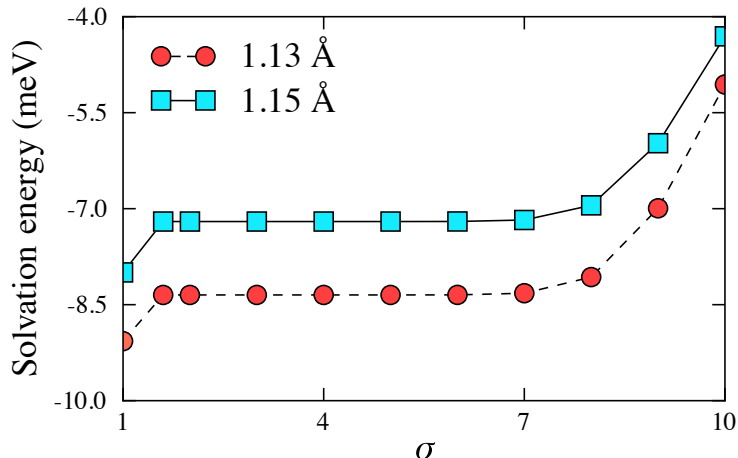


Figure 2.2: Solvation energy as function of the Gaussian ionic width for CO molecule for two different atomic separations, where the Gaussian width, σ , is specified in units of the grid size.

interaction energy does not depend on the Gaussian width. Figure 2.2 illustrates for the CO molecule that the solvation energy is independent of the choice of σ over a range of values of σ . For small values of σ , i.e. when σ is of the order of the grid spacing or smaller, deviations occur because of the reduced numerical accuracy of the integration of the Gaussians. For large values of σ , the deviations are caused by the Gaussians reaching into the region of the solvent.

For DFT implementations that use pseudopotentials such as VASP, [56] PWSCF, [37] ABINIT, [38] JDFTx, [95] *etc*, the electronic charge density corresponds only to the valence charge density which tapers off close to the atomic cores. Since the solvent effects described by the permittivity are assumed to be a functional of the local electronic charge density, the possibility exists that, due to the reduced valence charge density near the cores, the relative permittivity could become greater than one in the region of the atomic cores. Following Ref. [[60]], in order to ward off such unphysical solvent penetration into the atomic core regions, pseudo-charges centered at the atomic cores are added to

the valence charge density. This is strictly a numerical device and has no effect on the interaction energies as these pseudo charges are only used in the computation of the relative permittivity of the solvent. In principle, one could also replace these pseudo-charges with the partial core charges from an appropriately chosen pseudopotential, as is done in the current JDFTx implementation of the same fluid model. [95]

The generalized Poisson equation, Eq. (2.12), is solved using a preconditioned conjugate gradient algorithm. We use a pre-conditioner of the form $\frac{1}{G^2}$, where G is the nonzero reciprocal lattice vector. This choice of preconditioner gives the exact solution to the Poisson equation in Fourier space when the permittivity is constant.

The solution procedure using the conjugate gradient algorithm is made efficient through the use of FFTs for the evaluation of the gradient and divergence terms in Eq. (2.12). First, the gradient term, $\nabla\phi$, is evaluated in Fourier space. It is then transformed to real space and multiplied with the spatially varying permittivity, $\epsilon(\vec{r})$, which is given as a functional of the charge density. Then the divergence of the term $\epsilon(\vec{r})\nabla\phi$ is computed in the Fourier space using a FFT, leading to the complete Fourier space representation of the right hand side of Eq. (2.12).

For the shape function parameters n_c and σ in Eq. (2.11) and the effective surface tension τ in Eq. (2.8) we use the values of Ref. [[41]] that were obtained by a fit of the model to experimental solvation energies for molecules in water. The specific values are $n_c = 0.0025\text{\AA}^{-3}$, $\sigma = 0.6$, and $\tau = 0.525\text{meV}/\text{\AA}^2$. Using a hydrogen atom in a 10\AA cubic box as a test case, the effective surface area computed using Eq. (2.14) with $\sigma = 0.6$ agrees within 2% with the geometri-

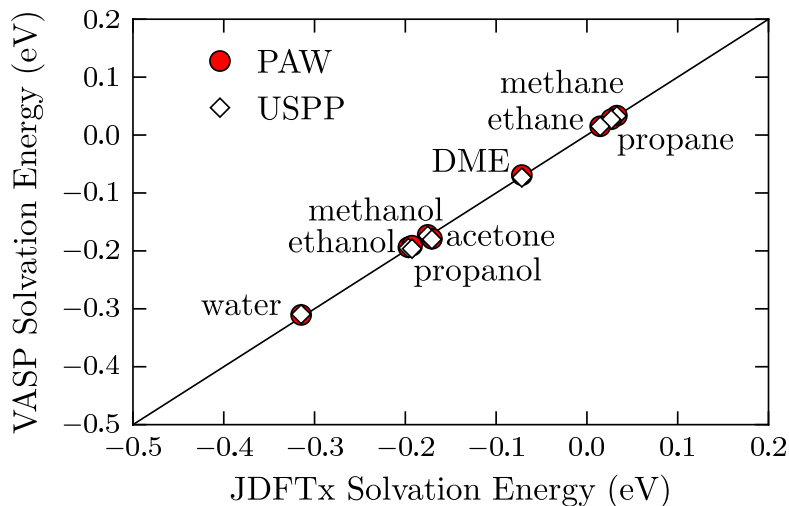


Figure 2.3: Comparison of solvation energies for different molecules in water calculated with VASP and JDFTx. The JDFTx calculations employed norm-conserving pseudopotentials and the VASP calculations ultrasoft pseudopotentials and the PAW method.

cal surface area at the cut-off charge density, n_c . Since the parameters used in the model are fit together, this small deviation is inconsequential and largely absorbed in the effective surface tension parameter τ .

The implementation of this solvation model in VASP is parallelized over multiple processors using MPI. To demonstrate the efficiency of the implementation, we calculate the surface energy of a Pt (111) surface slab with 5 layers of Pt and a 10 Å slab spacing. The vacuum SCF calculation, starting from random wavefunction, converged in 39 seconds and required 28 self-consistent iterations. The same system solvated in water, starting from the vacuum wave functions, converged in 35 seconds and required 16 self-consistent iterations. These calculations were performed on 4 nodes, each consisting of two 8-core Intel Xeon E5 processors, on the Texas Advanced Computing Center (TACC) Stampede system.

2.5 Validation of implicit solvation model

We validate the correct implementation of our solvation model for the energies and forces by comparing the solvation energies of several molecules with values obtained for the same solvation model from the JDFTx code [95] and with experimental results. For the forces, we compare the values from the implemented analytic expressions with the values obtained by numerical differentiation of the energy.

The calculations for the validation in this section as well as the applications in Sec. 2.6 are performed with the modified VASP code using USPP and the PAW method, the PBE exchange-correlation functional. For the molecular systems we use a cutoff energy of 800 eV, the Γ point for k -point sampling, and a cubic box of 10 Å edge length. The atomic positions are obtained from the computational chemistry comparison and benchmark database. [83] The calculations of the surface energies use a cutoff energy of 460 eV, a $16 \times 16 \times 1$ mesh for k -point sampling, and a vacuum spacing of 10 Å. The geometry of the platinum slabs for different crystal facets are taken from our previous study given in Ref. [[34]]. For PbS, 100 surface geometry had 5 layers, 110 had 10 layers and 111 had 9 layers (reconstructed surface with Pb termination). Fully relaxed vacuum slab geometries were used for both Pt and PbS solvation calculations. For the solvation model parameters, we use the default values of our implementation as specified in the previous section and the relative permittivity of water $\epsilon_b = 80$, which is the default solvent in the implementation.

The correctness of the VASP implementation of the solvation model is verified by comparing the solvation energies of organic molecules with the val-

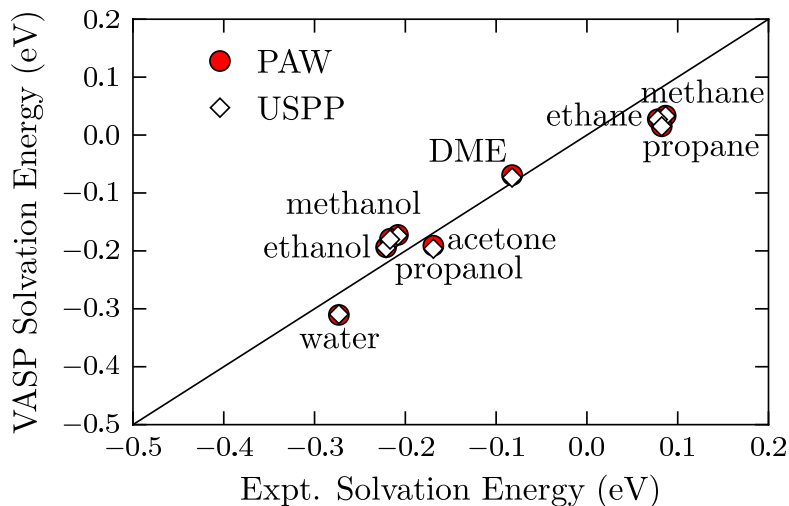


Figure 2.4: Experimental versus VASP calculated solvation energies for different molecules in water

ues obtained from the identical solvent model implemented in the JDFTx code. Figure 2.3 shows that the solvation energies of both codes are nearly identical, indicating that the method is implemented correctly. The small discrepancies between the VASP and JDFTx solvation energies (on the order of 10 meV) can be attributed to differences in the pseudopotentials used and are well within common pseudopotential errors. [75] Figure 2.4 compares the calculated solvation energies to experimental data. The calculated solvation energies are in good agreement with the experimental values. The experimental and computed solvation energies obtained using JDFTx and VASP are also listed in Table 2.1.

The implicit solvation model results in correction terms for the forces, which are derived from the energy expression of Eq. (2.9) and given by Eq. (2.14). We confirmed the numerical accuracy of the forces by comparing the results of the implemented analytic expressions with the values obtained by numerical differentiation of the energy for several molecules.

Table 2.1: Molecular solvation energies; VASP, JDFTx and experimental values. All energies are in eV

Molecules	E_{expt}	E_{jdfdx}	$E_{\text{VASP}}^{\text{PAW}}$	$E_{\text{VASP}}^{\text{USPP}}$
Acetone	-0.17	-0.19	-0.19	-0.20
Dimethyl ether	-0.08	-0.07	-0.07	-0.07
Ethane	+0.08	+0.03	+0.03	+0.03
Ethanol	-0.22	-0.17	-0.18	-0.18
Methane	+0.08	+0.01	+0.02	+0.01
Methanol	-0.22	-0.20	-0.19	-0.19
Propane	+0.09	+0.03	+0.03	+0.03
Propanol	-0.21	-0.18	-0.17	-0.17
Water	-0.27	-0.31	-0.31	-0.31

2.6 Applications

We apply the implemented solvation model to surfaces of materials that are of current technological interest and study the effect of various solvents on the surface energies of the dominant facets of metal and semiconductor nanocrystals. In addition, we determine the energy barrier for the nucleophilic substitution reaction of chloromethane and compare the results with quantum chemistry calculations.

2.6.1 Solvation effects on metal and semiconductor nanocrystals

Optical, electronic, and magnetic properties of nanocrystals strongly depend on their size and shape. These properties are in turn affected by the functional groups present on the surface and the type of solvent in which they are dispersed. Here we consider platinum and lead sulphide nanocrystals to ascertain how the presence of a solvent affects the surface energies of different nanocrystal facets and what the implications are for the nanocrystal shape. Platinum nanocrystals have a wide range of applications in catalysis from fuel cells to catalytic converters. [59, 17] Lead sulphide nanocrystals have exceptional optical properties [9] and are considered as emerging novel materials for inorganic-organic bulk hybrid solar cells [104] and tunable near infrared detectors. [76]

Figures 2.5 and 2.6 show how the presence of solvent affects the surface energies of the low-energy facets of Pt and PbS nanocrystals. In all cases, the solvent reduces the surface energies with the more polar solvents resulting in higher reductions. The reduction in surface energies for Pt are up to $2 \text{ meV}/\text{\AA}^2$ and for PbS up to $7 \text{ meV}/\text{\AA}^2$. The more significant effect of solvation on the PbS surfaces than the Pt surfaces is due to the nature of bonding in these systems. PbS exhibits a partially ionic bonding, while the Pt bonding is purely metallic. The presence of partially ionic bonds on the PbS surfaces lead to stronger electric fields at the surface experiencing solvent screening. Due to the reasonably high electric fields present at the PbS surfaces, we also confirm that a linear dielectric response to electric field strength is sufficient for capturing the solvation energy of these materials. For the PbS surfaces, the surface energy differences between the linear and nonlinear model calculated with the JDFTx code [41] is less than

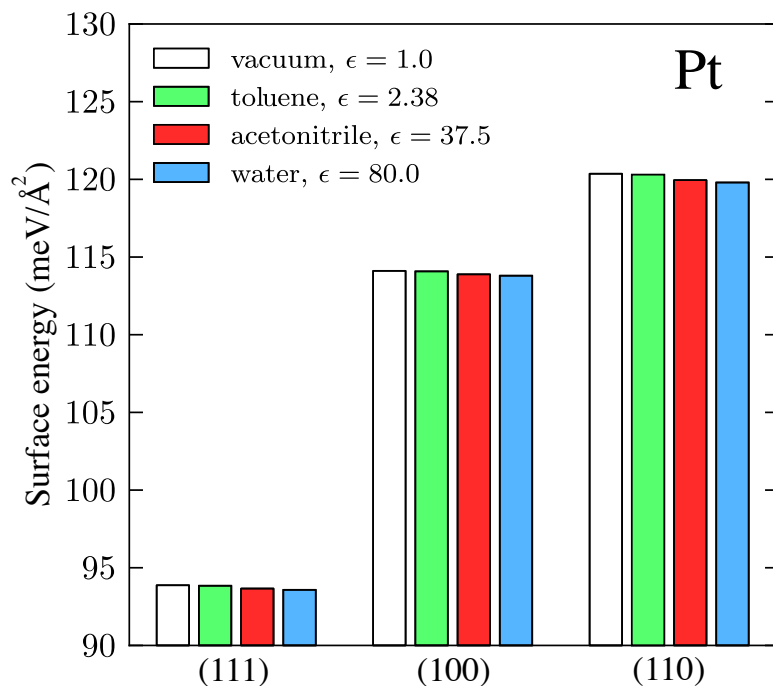


Figure 2.5: Surface energies of the (111), (100), and (110) facets of Pt nanocrystals in different solvents.

2%. Ref. [[41]] has confirmed that the effect of nonlinearity is also negligible for metal surfaces.

We observe that the surface energies of all facets are reduced by the electrostatic screening of the solvent, an effect which is particularly noticeable for the surfaces of the ionic PbS compound. While the absolute surface energies of PbS are significantly reduced by the presence of water, the change of the ratios of the surface energies with respect to the lowest energy facet, $\frac{\gamma_{(hkl)}}{\gamma_{(100)}}$, is significantly smaller. In the presence of the solvent, the surface energies become slightly more similar to each other. However, we find that the resulting effect of the solvent on the morphology of bare nanoparticles is negligible. In many synthesis processes, the nanoparticle morphology is also determined by the nature of the passivating ligands adsorbed on the surface and the rate at which they are ad-

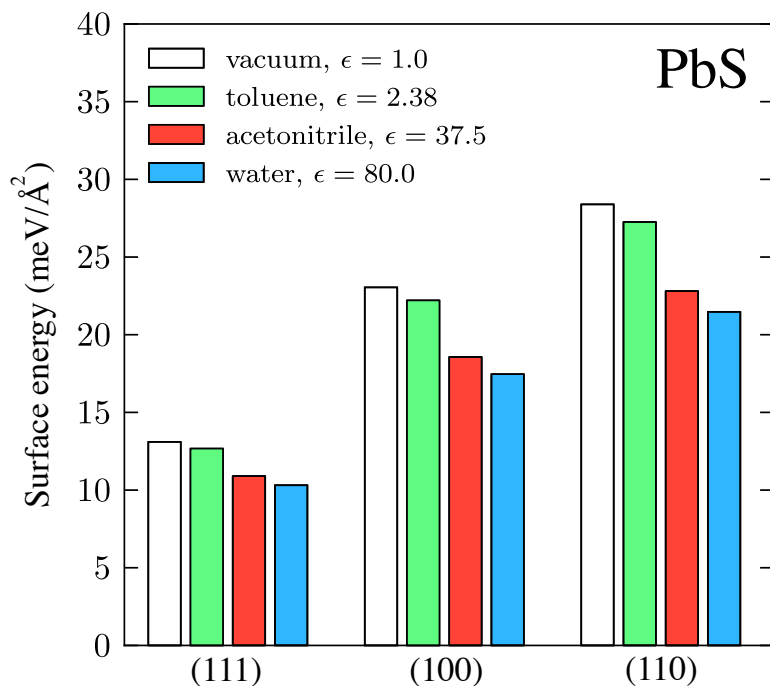


Figure 2.6: Surface energies of the (100), (111), and (110) facets of PbS nanocrystals in different solvents.

sorbed. [14, 12] The predicted change in the surface energies due to the presence of the solvents used during synthesis is expected to affect the energetics and the rate of ligand adsorption.

2.6.2 Reaction pathways

Reaction pathways and barriers are also influenced by the presence of solvents. [51, 84] To demonstrate the importance of solvation effects in determining the reaction pathways and to illustrate the capability of the current implementation, we consider the nucleophilic substitution S_N2 reaction of Cl^- and CH_3Cl . This bimolecular nucleophilic substitution plays an important role in physical organic chemistry and hydration increases the reaction energy barrier, which

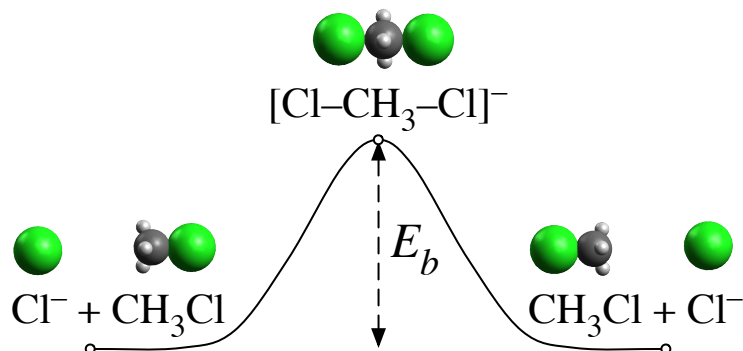


Figure 2.7: Nucleophilic substitution S_N2 reaction of a chlorine ion with chloromethane.

Table 2.2: Energy barriers for the nucleophilic substitution S_N2 in vacuum and in water calculated with VASP, Gaussian09, and constrained *ab-initio* molecular dynamics.

	E_b^{vacuum} (eV)	E_b^{water} (eV)
VASP	0.34	0.60
Fattebert and Gygi ¹		0.61
Gaussian09 ²	0.32	0.63
Gaussian 09 ³	0.32	0.69
<i>ab-initio</i> molecular dynamics ⁴		0.82

increases the the transfer rate by 20 orders of magnitude. [98]

Figure 2.7 illustrates the pathway for the S_N2 reaction $\text{Cl}^- + \text{CH}_3\text{Cl} \rightleftharpoons \text{ClCH}_3 + \text{Cl}^-$, where E_b is the energy barrier. We calculate the energy barriers for this reaction in vacuum and water using VASP and Gaussian09. [36] The VASP calculations employ a cutoff energy of 800 eV and our implemented solvation model. We place the molecules in a cubic box of 25 Å size, which we found sufficient for the convergence of the energy differences to an accuracy of 10 meV. The Gaussian09 calculations use the aug-cc-pV5Z basis set and the static isodensity

solvation model, [35] which is similar to the solvation model we implemented in VASP.

Table 2.2 compares the energy barrier for the S_N2 reaction obtained with VASP with various other methods. We find that the energy barriers obtained from VASP and Gaussian09 are in good agreement. We also observe that the energy barrier in Gaussian09 only weakly depends on the solvation model. The energy barriers obtained with our solvation model in VASP and Gaussian09 also compare well with the result of Fattebert and Gygi [31] of 0.61 eV which neglected the contribution from the cavitation. [31] For the case of this reaction energy barrier, neglecting the cavitation energy is a good approximation since the cavity does not change much during the reaction. The reaction barrier obtained with constrained *ab-initio* molecular dynamics simulations with explicit solvent is 0.82 eV [30], about 0.2 eV higher than the values for the implicit solvation model. This difference may be due to anharmonic contributions to the energy barrier.

2.7 Conclusions

We implemented an implicit solvation model that describes the effect of electrostatics, [79] cavitation, and dispersion [5] on the interaction between a solute and solvent into the plane-wave DFT code VASP. The model was validated by comparing the values from the VASP implementation with the values from the JDFTx implementation and experimental data. Our implementation provides a computationally efficient means to calculate the effects of solvation on molecules and crystal surfaces. We apply the solvation model to deter-

mine the effects of solvation on the different facets of metal and semiconductor nanocrystals and the energy barrier for the nucleophilic substitution reaction of chloromethane. Solvation significantly reduces the surface energies of the semiconducting PbS nanocrystals and only weakly affects the surface energies of the metallic Pt nanocrystals. For the nucleophilic substitution reaction we obtain energy barriers in good agreement with previous calculations. The strength of our solvation model implementation is its capability to handle large periodic systems such as metal and semiconductor surfaces and its interoperability with standard ultrasoft pseudopotential and projector-augmented wave potential libraries. The software is freely available as a patch to the original VASP code. [66]

CHAPTER 3

IMPLICIT SELF-CONSISTENT DESCRIPTION OF ELECTROLYTE IN PLANE-WAVE DENSITY-FUNCTIONAL THEORY¹

3.1 Abstract

Ab-initio computational treatment of electrochemical systems requires an appropriate treatment of the solid/liquid interfaces. A fully quantum mechanical treatment of the interface is computationally unfeasible due to the large number of degrees of freedom involved. In this work we describe a computationally efficient model where the electrode part of the interface is modeled at the density functional theory (DFT) level and the electrolyte part is represented through an implicit model based on the Poisson-Boltzmann equation. We describe the implementation of the model Vienna Ab-initio Simulation Package (VASP), a widely used DFT code, followed by validation and benchmarking of the implementation. To demonstrate the utility of the implicit electrolyte model we apply the model to study the effect of electrolyte and external voltage on the surface diffusion of sodium atoms on the electrode.

3.2 Introduction

Interfaces between dissimilar systems are ubiquitous in nature and frequently encountered and employed in scientific and engineering applications. Of particular interest are solid/liquid interfaces that form the crux of many tech-

¹To be published as 'Kiran Mathew and R. G. Hennig, Implicit self-consistent description of electrolyte in plane-wave density-functional theory'

nologically important systems such as electrochemical interfaces, [102, 43, 63] nanoparticle synthesis, [24, 70, 64] and protein folding and membrane formation. [28] A comprehensive understanding of the behavior and properties of such systems requires a detailed microscopic description of the solid/liquid interfaces.

Given the heterogeneous nature and the complexities of solid/liquid interfaces, [2] it is often the case that experimental studies need to be supplemented by theoretical undertakings. A complete theoretical study of such interface based on an explicit description of the electrolyte and solute involves solving systems of nonlinear equations with enormous amount of degrees of freedom and quickly become prohibitively expensive even when state of the art computational resources are employed. [47] This calls for the development of efficient implicit computational frameworks for the study of solid/liquid interfaces. [105, 47, 79, 25, 62, 5]

We have previously developed a self-consistent solvation model [68, 67] that describes the dielectric screening of a solute embedded in an implicit solvation model for the solvent, where the solute is described by density-functional theory (DFT). We implemented this solvation model into the widely used DFT code VASP. [56] This software package, VASPsol, is freely available under the GPL v3 license and has been used by us and others to study the effect of the presence of solvent on a number of materials and processes, such as the catalysis of ketone hydrogenation, [69] the interfacial chemistry in electrochemical interfaces, [58] hydrogen adsorption on platinum surfaces, [85] *etc.*

In this work we describe the extension of our solvation model VASPsol [68, 67] to include the effects of mobile ions in the solvent through the so-

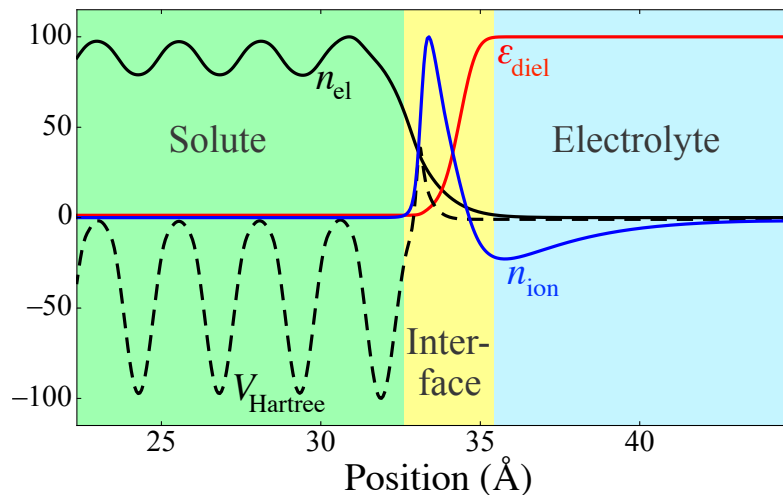


Figure 3.1: Spatial decomposition of the solid/electrolyte system into the solute, interface, and electrolyte regions for a bcc Na(110) surface embedded in an electrolyte with relative permittivity $\epsilon_r = 78.4$ and monovalent cations and anions with concentration 1M. The solute is described by density-functional theory, the electrolyte by an implicit solvation model. The interface regions is formed self-consistently as a functional of the electronic density of the solute. All properties are shown as a percentage of their maximum absolute value.

lution of the linear Poisson-Boltzmann equation and then apply the method to electrochemical systems to illustrate the power of this approach. Figure 3.1 illustrates how the solid/electrolyte system is divided into spatial regions that are described by the explicit DFT and the implicit solvation model. This new solvation model allows for the description of charged systems and the study of the electrochemical interfacial systems under applied external voltage. Section 3.3 describes the formalism and outlines the derivation of the energy expression. In Sec. 3.4 we describe the details of the implementation and validate the method against previous computational studies of electrochemical systems. Finally, in Sec. 3.5 we apply the method to study the effect of an applied external potential on the adsorption and surface diffusion for metal electrodes.

3.3 Theoretical framework

Our solvation model couples an implicit description of the electrolyte to a quantum-mechanical explicit description of the solute. The implicit solvation model incorporates the dielectric screening due to the permittivity of the solvent and the electrostatic shielding due to the mobile ions in the electrolyte. The solute is described explicitly using DFT.

To obtain the energy of the combined solute/electrolyte system, we spatially divide the materials system into three regions: (i) the solute that we describe explicitly using DFT, (ii) the electrolyte that we describe using the linear Poisson-Boltzmann equation and (iii) the interface region, that electrostatically couples the DFT and Poisson-Boltzmann equation. Fig. 3.1 illustrates the regions for a Na(110) surface embedded in a 1M aqueous electrolyte. The interface between the electrolyte and the solute system is formed self-consistently through the electronic density and the interaction between the electrolyte and solute is described by the electrostatic potential as explained in the following sections.

3.3.1 Total energy

We define the interface region between the solute and the electrolyte using the electronic charge density of the solute, $n(\vec{r})$. The electrolyte occupies the volume of the simulation cell where the solute charge density goes to zero. In the interface region where the electronic charge density increases rapidly from zero towards the average bulk value of the solute, the properties of the implicit solvation model, *e.g.* the permittivity ϵ and the Debye screening length

λ_D , change from their bulk values of the electrolyte to the vacuum values in the explicit region. The scaling of the electrolyte properties is given by a shape function [68, 60, 79, 95, 41]

$$S(n(\vec{r})) = \frac{1}{2} \operatorname{erfc} \left\{ \frac{\log(n/n_c)}{\sigma \sqrt{2}} \right\}. \quad (3.1)$$

Following our previous work [68] and the work by Arias *et al.*, [60, 79, 95, 41] the total free energy, A , of the system consisting of the solute and electrolyte is expressed as

$$\begin{aligned} A[n(\vec{r}), \phi(\vec{r})] &= A_{\text{TXC}}[n(\vec{r})] + \int \phi(\vec{r}) \rho_s(\vec{r}) d^3 r \\ &\quad - \int \epsilon(\vec{r}) \frac{|\nabla \phi|^2}{8\pi} d^3 r + \int \frac{1}{2} \phi(\vec{r}) \rho_{\text{ion}}(\vec{r}) d^3 r \\ &\quad + A_{\text{cav}} + A_{\text{ion}}, \end{aligned} \quad (3.2)$$

where A_{TXC} is the kinetic and exchange-correlation contribution from DFT, ϕ is the net electrostatic potential of the system, and ρ_s and ρ_{ion} are the total charge density of the solute and the ionic charge density of the electrolyte, respectively. The net solute charge density, ρ_s , is the sum of the solute electronic and nuclear charge densities, $n(\vec{r})$ and $N(\vec{r})$, respectively,

$$\rho_s(\vec{r}) = n(\vec{r}) + N(\vec{r}). \quad (3.3)$$

The net ionic charge density, ρ_{ion} , is given by

$$\rho_{\text{ion}}(\vec{r}) = \sum_i q z_i c_i(\vec{r}), \quad (3.4)$$

where $c_i(\vec{r})$ is the concentration of ionic species i with charge $z_i q$, and q is the elementary charge. The concentration of ionic species, c_i , is given by a Boltzmann factor of the electrostatic energy [89] and modulated in the interface region by the shape function, $S(n(\vec{r}))$,

$$c_i(\vec{r}) = S[n(\vec{r})] c_i^0 \exp \left(\frac{-z_i q \phi(\vec{r})}{kT} \right), \quad (3.5)$$

where c_i^0 is the bulk concentration of ionic species i , k is the Boltzmann constant and T the temperature. The relative permittivity of the electrolyte, $\epsilon(\vec{r})$, is assumed to be a local functional of the electronic charge density of the solute and modulated by the shape function, [68, 60, 79, 95, 41]

$$\epsilon(n(\vec{r})) = 1 + (\epsilon_b - 1)S(n(\vec{r})), \quad (3.6)$$

where ϵ_b is the bulk relative permittivity of the solvent. The cavitation energy, A_{cav} , describes the energy required to form the solute cavity inside the electrolyte and is given by [5]

$$A_{\text{cav}} = \tau \int |\nabla S| d^3r. \quad (3.7)$$

In comparison to our previous solvation model, [68] the main changes to the free energy expression are the inclusion of the electrostatic interaction of the ionic charge density in the electrolyte with the system's electrostatic potential, ϕ , and the non-electrostatic contribution to the free energy from the mobile ions in the electrolyte, A_{ion} . In this work we assume that to be just the entropic contribution, [89] *i.e.*

$$A_{\text{ion}} = kTS_{\text{ion}}, \quad (3.8)$$

where S_{ion} is the entropy of mixing of the ions in the electrolyte, which for small electrostatic potentials can be approximated to first order as

$$\begin{aligned} S_{\text{ion}} &= \int \sum_i c_i \ln\left(\frac{c_i}{c_i^0}\right) d^3r \\ &\approx - \int \sum_i c_i \frac{z_i q \phi}{kT} d^3r. \end{aligned} \quad (3.9)$$

3.3.2 Minimization

To obtain the stationary point of the free energy, A , given by Eq. (3.2), we set the first order variations of the free energy with respect to the system potential, ϕ , and the electronic charge density, $n(r)$, to zero. [68, 60, 79, 95, 41] Taking the variation of $A[n(\vec{r}), \phi(\vec{r})]$ with respect to the electronic charge density, $n(\vec{r})$, yields the typical Kohn-Sham Hamiltonian [55] with the following additional term in the local part of the potential

$$V_{\text{solv}} = \frac{\delta\epsilon(n)}{\delta n} \frac{|\nabla\phi|^2}{8\pi} + \phi \frac{\delta\rho_{\text{ion}}}{\delta n} + \tau \frac{\delta|\nabla S|}{\delta n} + kT \frac{\delta S_{\text{ion}}}{\delta n}. \quad (3.10)$$

Taking the variation of $A[n(\vec{r}), \phi(\vec{r})]$ with respect to $\phi(\vec{r})$ yields the generalized Poisson-Boltzmann equation

$$\vec{\nabla} \cdot \epsilon \vec{\nabla} \phi = -\rho_s - \rho_{\text{ion}}, \quad (3.11)$$

where $\epsilon(n(r))$ is the relative permittivity of the solvent as a functional of the electronic charge density.

We further simplify the system by considering the case of electrolytes with only two types of ions present, whose charges are equal and opposite, *i.e.* $c_1^0 = c_2^0 = c^0$ and $z_1 = -z_2 = z$. Then the ionic charge density of the electrolyte becomes [89]

$$\begin{aligned} \rho_{\text{ion}} &= qzc^0 \left[\exp\left(\frac{-zq\phi}{kT}\right) - \exp\left(\frac{zq\phi}{kT}\right) \right] \\ &= -2qzc^0 \sinh\left(\frac{zq\phi}{kT}\right) \end{aligned} \quad (3.12)$$

and the Poisson-Boltzmann equation becomes

$$\vec{\nabla} \cdot \epsilon \vec{\nabla} \phi = -\rho_s + 2qzc^0 \sinh\left(\frac{zq\phi}{kT}\right). \quad (3.13)$$

For small arguments $x = \frac{zq\phi}{kT} \ll 1$, $\sinh(x) \rightarrow x$ and we obtain the linearized Poisson-Boltzmann equation

$$\vec{\nabla} \cdot \epsilon \vec{\nabla} \phi - \kappa^2 \phi = -\rho_s \quad (3.14)$$

with

$$\kappa^2 = \left(\frac{2c^0 z^2 q^2}{kT} \right) = \frac{1}{\lambda_D^2}, \quad (3.15)$$

where λ_D is the Debye length that characterizes the dimension of the electrochemical double layer.

3.4 Implementation and validation

The implicit electrolyte model described above is implemented in the widely used DFT software Vienna Ab-initio Software Package (VASP). [56] VASP is a parallel plane-wave DFT code that supports both ultra-soft pseudopotentials [100, 57] as well as the PAW [18] formulation of pseudopotentials.

The main modifications in the code are the evaluation of the additional contributions to the total energy and the local potential given by Eqs. (3.2) and (3.10), respectively. Corrections to the local potential require the solution of the generalized Poisson-Boltzmann equation (3.13) in each self-consistent iteration. Our implementation solves the equation in reciprocal space and makes efficient use of fast Fourier transformations (FFT). [68] This enables our implementation to be compatible with the Message Passing Protocol (MPI) and to take advantage of the memory layout of VASP. We use a pre-conditioned conjugate gradient algorithm to solve the generalized Poisson-Boltzmann equation with the pre-conditioner $(G^2 + \kappa^2)^{-1}$, where G is the magnitude of the reciprocal lattice

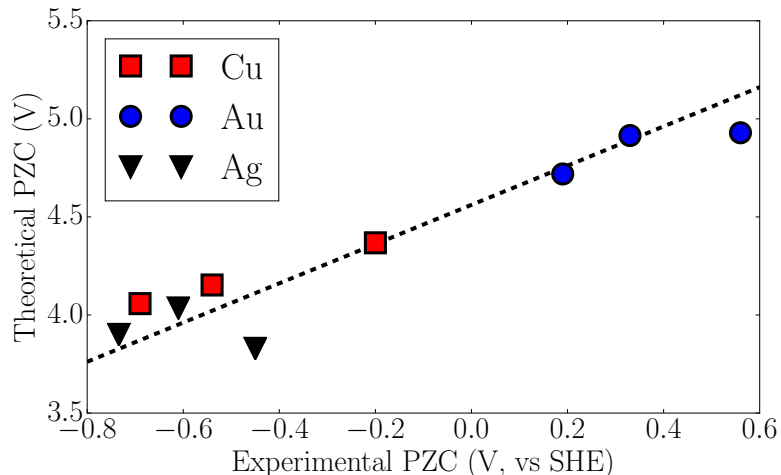


Figure 3.2: Comparison between the computed and the experimental Potential of Zero Charge (PZC) with respect to the standard hydrogen electrode (SHE). The dashed line is a fit of $V^{\text{pred}} = V^{\text{exp}} + V_{\text{SHE}}^{\text{pred}}$ to determine the theoretical potential of the SHE.

vector and κ^2 is the inverse of the square of the Debye length, λ_D . Our software module, VASPsol, is freely distributed as an open-source package and hosted on GitHub at <https://github.com/henniggroup/VASPsol>. [67]

We benchmark the model against existing experimental and computational data. [60] First, we compute the potential of zero charge (PZC) of various metallic slabs and compare them against the experimental values. Second, we compute the surface charge density of a Pt(111) slab as function of the applied external potential and compare the resulting value of the double layer capacitance with previous computation and experiment.

The DFT calculations for these two benchmarks are performed with VASP and the VASPsol module using projected augmented wave (PAW) formalism describing the electron-ion interactions and the PBE approximation for the exchange-correlation functional. [56, 77] The Brillouin-zone integration uses an $8 \times 8 \times 1$ k -points. A high plane-wave basis set cutoff energy of 800 eV is used

to ensure proper resolution of the interfacial region between the solute and implicit. We consider an electrolyte that consists of an aqueous solution of monovalent anions and cations of 1M concentration. At room temperature this electrolyte has a relative permittivity of $\epsilon_b = 78.4$ and a Debye length of 3 \AA . To change the applied potential, we adjust the electron count and then determine the corresponding potential from the shift in electrostatic potential as reflected in the shift in Fermi level. This takes advantage of the fact that the electrostatic potential goes to zero in the electrolyte region for the solution of the Poisson-Boltzmann equation.

Figure 3.2 compares the electrode potential of zero charge (PZC) calculated with the implicit electrolyte model as implemented in VASPsol with experimental data. The electrode potential of zero charge is defined as the electrostatic potential of a neutral metal electrode and is given by the Fermi energy with respect to a reference potential. A natural choice of reference for the implicit electrolyte model is the electrostatic potential in the bulk of the electrolyte, which is zero in any solution of the Poisson-Boltzmann equation. In experiments, the reference is frequently chosen as the standard-hydrogen electrode (SHE). The dashed line in Fig. 3.2 presents the fit of $V^{\text{pred}} = V^{\text{exp}} + V_{\text{SHE}}^{\text{pred}}$ to obtain shift between the experimental PZC and the computed PZC, . *i.e.* the potential of the SHE for our electrolyte model. The resulting $V_{\text{SHE}}^{\text{pred}} = 4.6 \text{ V}$ compares very well with the previously reported computed value of 4.7 V for a similar solvation model. [41]

Figure 3.3 shows the calculated surface charge density, σ , of the Pt (111) surface as a function of applied electrostatic potential, V . The linear slope of $\sigma(V)$ is the double-layer capacitance. The resulting double-layer capacitance for the Pt (111) surface at 1M concentration is $15 \mu\text{F}/\text{cm}^2$, which closely agrees

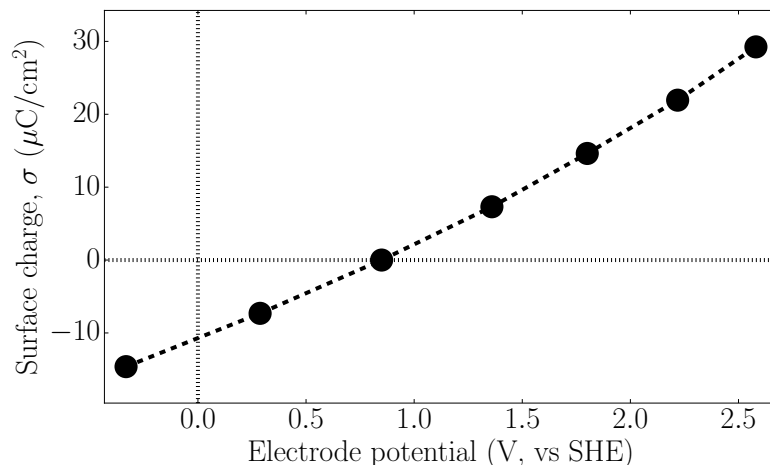


Figure 3.3: Surface charge density of the Pt (111) surface as a function of applied electrostatic potential computed with the implicit electrolyte module, VASPsol. The slope of the curve determines the capacitance of the dielectric double layer.

with the previously reported computed [41] and experimental [99] values of $14 \mu\text{F}/\text{cm}^2$ and $20 \mu\text{F}/\text{cm}^2$, respectively. The discrepancy between the VASPsol value of the double layer capacitance and the computed value in the literature can be attributed to the difference in pseudo-potentials.

3.5 Applications

The implicit electrolyte model, VASPsol, enables the study the electrode surfaces in realistic environments and under various conditions, such as of an electrode immersed in an electrolyte with an external potential applied. To illustrate the utility of the solvation model, we apply it to study the adsorption energy and diffusion energy barrier of an adatom on a metallic electrode that is immersed in a 1M aqueous electrolyte as a function of applied potential.

Stability of fuel cell materials plays a significant role in the the development

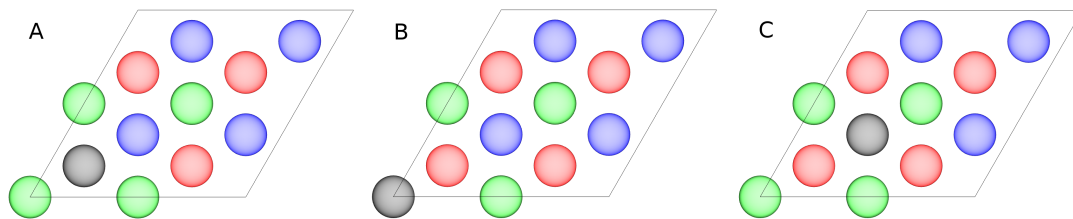


Figure 3.4: Pt adatom(black) adsorbed on three different sites on the Pt 111 surface. Red, green and blue indicate top, second and third layers of Pt 111 respectively

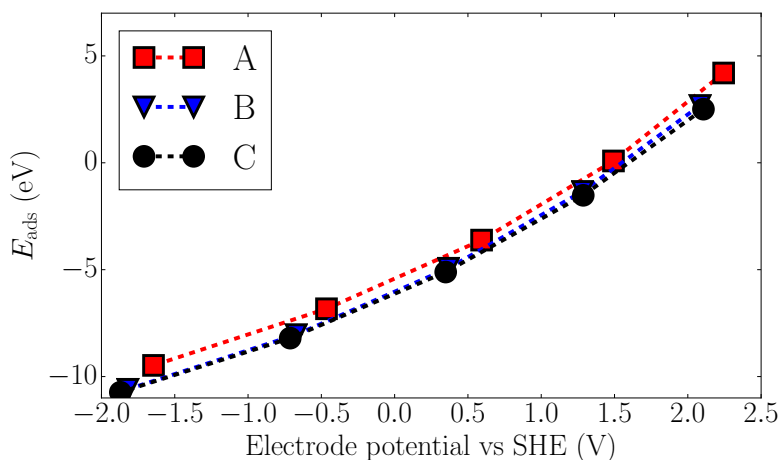


Figure 3.5: Plot of voltage vs the adsorption energy

of polymer electrolyte fuel cells (PEFCs). PEFC performance loss under steady-state and cycling conditions has been attributed in part to a loss of electrochemically active surface area of the platinum cathode electro-catalyst [103]. In this work we study the dissolution of Pt electrode by looking at the adsorption energies of Pt adatom on Pt 111 surfaces. We apply the implicit electrolyte model to simulate the Pt electrode under external potential. For the adsorption, three adsorption sites are considered, labeled A, B and C, as shown in Figure 3.4. The plot of adsorption energy as a function of the externally applied potential is shown in the Figure 3.5. From the plot it can be observed that the adsorption energy increases as the potential is ramped up. This implies that the Pt adatom is

less likely to adsorb on to the Pt 111 surface at higher potentials i.e rate of dissolution is higher at larger potentials. The observation is corroborated by previous experimental studies [32, 103], thus demonstrating the practical applicability of the model.

3.6 Conclusions

Solid/liquid interfaces between electrodes and electrolytes in electrochemical cells present a complex system that requires the insights provided by computational studies to supplement and explain experimental observations. We developed and implemented a self-consistent computational framework that provides an efficient implicit description of electrode/electrolyte interfaces within density-functional theory through the solution of the generalized linear Poisson-Boltzmann equation. The electrolyte model is implemented in the widely used DFT code VASP and the implementation is made available as a free and open-source module, VASPsol. We show that this model enables ab-initio studies of electrochemistry at the DFT level. We validate the model by comparing the calculated electrode potential of zero charge for various metal electrodes with experimental values and by comparing the calculated double-layer capacitance of Pt (111) in a 1M solution and to previously calculations and experiments. To illustrate the usefulness of the model and the implementation, we compute the adsorption energy of Pt adatoms on a Pt (111) electrode as function of the applied potential. Confirming previous experimental observations, we find that the Pt dissolution rate increases as a function of the externally applied potential.

CHAPTER 4
SELF-CONSISTENT NON-LINEAR SOLVATION MODEL IN
PLANE-WAVE DENSITY-FUNCTIONAL THEORY ¹

4.1 Abstract

The accurate computational description of electrochemical interfaces requires a description of a wide range of physical phenomena occurring at the electrode/-electrolyte interfaces. Implicit solvation models provide a simple, yet powerful method to account for solvation effects. One particular aspect encountered in electrochemical applications is the dielectric saturation of the permittivity at high electric fields near the interfaces. In this work we describe a computationally efficient self-consistent implicit solid/liquid interface model within the density-functional theory framework that accounts for dielectric saturation. The model is implemented in the widely used Vienna Ab-initio Simulation Package (VASP). The usefulness of the implementation is demonstrated by applying the model to compute the surface energies of highly ionic solid surfaces. We show that the non-linear response of the solvent increases the surface energy relative to a linear model and avoids unphysical negative surface energies.

4.2 Introduction

The surface chemistry of solid/liquid interfaces affects many fundamental processes such as the synthesis and self-assembly of nanoparticles, the structures of

¹To be published as 'Kiran Mathew, R. Sundararaman, D. Gunceler, T. A. Arias and R. G. Hennig, Self-consistent non-linear solvation model in plane-wave density-functional theory'

protein complexes, and the performance of electrochemical cells and heterogeneous catalysts. [2, 12, 64, 28] Experimental methods alone can seldom provide a complete insight into the characterization of these interfaces. A complementary route to the understanding and the design of solid/liquid interfaces is to supplement experimental efforts with appropriate computational studies.

The computational treatment of solvated systems can be categorized into two types of approaches that are based on if the solvent effects are modeled explicitly or implicitly. [25] Explicit solvation models can account for all degrees of freedom of the solvent molecules. This can become computationally demanding, as proper thermodynamic averaging requires a large number of solvent molecules and sufficiently long simulation times. Implicit models, on the other, account for the solvent effects through the average equilibrium properties of the solvent. This reduces the computational expenses considerably but potentially at the expense of chemical accuracy. Therefore caution must be taken in developing and choosing implicit models for an accurate description of the solid/liquid interfaces of interest. [97]

To the first order the solvent effects can be accounted for by including only the electrostatic effects between the solute and solvent. [6, 47] This coupled with a polarization that is proportional to the system electric field constitutes the linear solvation model. [31, 5] The model has been shown to be efficient and reasonably accurate for a multitude of systems. [60, 79, 68, 5] However, the linear model fails to account for phenomena, such as the dielectric saturation observed in solvents at high electric fields. Such high fields are in fact abundant in typical systems of interest such as at the solid electrolyte interfaces (SEI) in electrochemical systems.

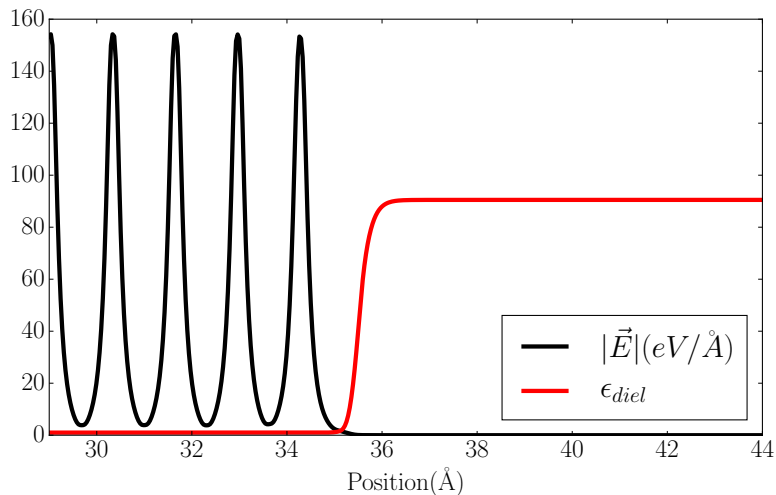


Figure 4.1: Plot of $|\vec{E}|$, the magnitude of the electric field averaged over x-y plane, and the relative permittivity, averaged over x-y plane, for LiF 100 surface in Ethylene Carbonate solvent computed using the nonlinear solvation model.

Solvation models that account for the nonlinear effects such as the dielectric saturation phenomenon by including electric field dependent relative permittivity in the solving of the electrostatic potential has been developed in the past and been applied to study the protein structure [3]. The joint DFT developed by Arias *et al.* puts the nonlinear effects: dielectric saturation and the finite ion size effects into a density-functional theory (DFT) perspective. [41] In this work we present a nonlinear solvation model that is based of the work by Arias.et.al and puts it in a self-consistent framework. The model is implemented in the DFT code VASP and the module, VASPsol, [68, 67] is made freely available. This extends the capabilities of the VASPsol framework that already implements an efficient self-consistent linear solvation model to incorporate the nonlinear effects.

The paper is organized as follows: In section 4.3 we briefly describe the theoretical framework and derive the modified Kohn-Sham Hamiltonian. In sec-

tion 4.3 and section 4.4 we describe the self-consistent implementation of the model into the widely used DFT code VASP and validate and benchmark the implementation by comparing the results obtained using the implementation (VASPsol) against previously reported computed values as well as experimental values. In section 4.5 we demonstrate the usefulness of this model by applying it to study the solvent effects on the facets of ionic crystals. We find that the nonlinear model succeeds in rectifying the unphysical effects produced by the linear model under extreme conditions.

4.3 Theoretical framework

Following previous work [41], in the following subsections we first derive the total free energy of the solute/solvent system and then minimize it to obtain the ground state. The highlight of this work, putting the implicit nonlinear model in a self consistent framework, is emphasized in the second subsection with detailed derivations and discussions.

4.3.1 Total energy

We divide the materials system into two spatial regions, (i) the solute part of the system that we describe explicitly using density-functional theory (DFT) and the solvent part that we describe using an implicit model. The total free energy

of the combined solute-solvent system is given by

$$A_{\text{tot}}[n(\vec{r}), e(\vec{r})] = A_{\text{solute}}[n(\vec{r})] + A_{\text{solvent}}[n(\vec{r}), e(\vec{r})] + A_{\text{interface}}[n(\vec{r})] \quad (4.1)$$

where $n(\vec{r})$ is the electronic charge density of the solute and $e(\vec{r})$ is the non-dimensional electric field. In the next section we show how $e(\vec{r})$ is related to the system electric field \vec{E} through a nonlinear transformation.

The solute contribution, A_{solute} , as a functional of the electronic charge density is given by the Hohenberg-Kohn functional

$$A_{\text{solute}}[n(\vec{r})] = A_{\text{TXC}}[n(\vec{r})] + \frac{1}{2} \int \phi(\vec{r}) \rho_s(\vec{r}) d^3r,$$

where A_{TXC} describes the kinetic and exchange-correlation energy contributions and the second term provides the electrostatic energy. In the above expression, ϕ is the electrostatic potential due all the charges in the solute/solvent system and ρ_s is the total solute charge density, *i.e.* $\rho_s = n + n_{\text{ion}}$ where n is the electronic charge density and n_{ion} the nuclear charge density.

In this work we assume that the solvent is composed of dipoles that feel the presence of the rest of the solvent and the solute through the system electrostatic potential ϕ and the non-dimensional electric field e . The non-dimensional electric field does not exactly correspond to the electric field derived directly from the gradient of the system potential. Its relation to the system potential will be made clear in the next section. With that approximation, the solvent contribution, A_{solvent} , is further broken down into the dielectric medium energy, A_{dm} , which accounts for the energy of the solvent dipoles in the presence of the rest of the solvent and the electrostatic energy of the bound charges induced in the

solvent.

$$A_{\text{solvent}}[n(r), e] = A_{\text{dm}}[n(r), e] + A_{\text{el}}[n(r), e]$$

The dielectric medium energy, A_{dm} , as a functional of electronic charge density, $n(r)$ and the electric field e is given by [41]

$$\begin{aligned} A_{\text{dm}}[n(r), e] = & \\ & k_B T \int S(n(r)) N_{\text{sol}} \left[e^2 \left\{ f(e) - \frac{\alpha}{2} f(e) \right\} - \log \frac{\sinh e}{e} \right] d^3 r \\ & + k_B T \int S(n(r)) N_{\text{sol}} \left[e^2 \frac{X}{2} (1 - \alpha f(e))^2 \right] d^3 r, \end{aligned}$$

where $ef(e) = \coth(e) - \frac{1}{e}$ is the Langevin function and N_{sol} is the number density of the solvent molecules. The first term in the above expression corresponds to the rotation contribution of the dipoles and the second term corresponds to the linear polarization. Constraining the parameters X and α to produce the static and high field limits of the dielectric constant, ϵ_b and ϵ_∞ , respectively, yields [41]

$$X = \frac{k_B T (\epsilon_\infty - 1)}{4\pi N_{\text{sol}} p_{\text{mol}}^2}$$

and

$$\alpha = 3 - \frac{4\pi N_{\text{sol}} p_{\text{mol}}^2}{k_B T (\epsilon_b - \epsilon_\infty)},$$

where p_{mol} is the dipole moment of the solvent molecule.

The shape function, $S(n(r))$, that defines the interface region between the solute and the solvent using the solute electronic charge density given by

$$S(n(\vec{r})) = \frac{1}{2} \operatorname{erfc} \left\{ \frac{\log(n_{\text{solute}}/n_c)}{\sigma \sqrt{2}} \right\}.$$

The interaction of the the bound charge, ρ_b , in the solvent with the electrostatic potential, ϕ , gives the solvent electrostatic energy contribution, A_{el}

$$A_{el}[n(r), e] = \frac{1}{2} \int \phi \rho_b d^3 r$$

The bound charge density, ρ_b is given by $-\nabla \cdot \vec{P}$, where \vec{P} is the polarization density.

Finally the interfacial contribution is taken to be the energy required to form the cavity in the solvent within which the solute is placed.

$$\begin{aligned} A_{\text{interface}}[n(r)] &= A_{\text{cav}}[n(r)] \\ &= \tau \int d^3 r |\nabla S(n(r))|, \end{aligned}$$

where τ is the effective surface tension parameter and $S(n(r))$ is the cavity shape functions defined above.

Combining all the above terms, the total free energy of the solute-solvent system becomes

$$\begin{aligned} A_{\text{tot}}[n(r), e] &= A_{\text{TXC}}[n(r)] + \frac{1}{2} \int \phi \rho_s d^3 r \\ &+ \frac{1}{2} \int \phi \rho_b d^3 r + A_{\text{dm}}[n(r), e] \\ &+ A_{\text{cav}}[n(r)]. \end{aligned}$$

Ionic contribution

The above model can be easily extended to include the effects of ions in the solution. This enables one to model electrolytes at the DFT level. The ionic contribution to the total energy, A_{ion} , constitutes the electrostatic contribution due to the ionic charge density and the entropy of mixing contribution from the

ions in the solution as well as the finite size effects of the ions described by the hard sphere model. The expression for A_{ion} is given by [41]

$$A_{\text{ion}}[n(r), \eta_i] = \frac{1}{2} \int \phi \rho_{\text{ion}}(n, \eta_i) d^3 r + k_B T \int s(n(r)) \sum_i N_i [\eta_i (\log \eta_i - 1) + 1 + \frac{(x - x_0)^2}{x_0(1 - x_0)^2(1 - x)^2}]$$

where N_i and η_i are the overall concentration and the local density of ionic species i in the electrolyte, respectively. The packing fraction $x(r)$ is given by,

$$x(r) = \sum N_i V_i \eta_i(r)$$

where V_i is the volume of the ionic species i and $x_0 = \sum N_i V_i$ is the bulk packing fraction.

Thus the total free energy of the solute-electrolyte system becomes

$$A_{\text{tot}}[n(r), e, \eta_i] = A_{\text{TXC}}[n(r)] + \frac{1}{2} \int \phi \rho_s d^3 r + \frac{1}{2} \int \phi \rho_b d^3 r + A_{\text{dm}}[n(r), e] + \frac{1}{2} \int \phi \rho_{\text{ion}}(n, \eta_i) d^3 r + A_{\text{ion}}[n(r), \eta_i] + A_{\text{cav}}[n(r)].$$

4.3.2 Self-consistent minimization

The total free energy expression for the solute/solvent system that we obtained above is minimized to obtain the ground state. To that end the first order variation of the the free energy functional with respect to the electronic charge density, $n(r)$ and the electric field, e are taken and then set to zero.

Starting from the expression for the total free energy, A_{tot} , adding and subtracting the Hartree energy of the solute system, the total energy can be written

as

$$\begin{aligned}
A_{\text{tot}}[n(r), e] = & A_{\text{TXC}}[n(r)] + \frac{1}{2} \int \phi_h \rho_s \\
& + \frac{1}{2} \int \phi(\rho_s + \rho_b) - \frac{1}{2} \int \phi_H \rho_s \\
& + A_{\text{dm}}[n(r), e] + A_{\text{cav}}[n(r)]
\end{aligned}$$

where ϕ_h is the potential due to ρ_s , the solute charge density. The first two terms correspond to the usual vacuum only free energy of the solute system. Grouping the first two terms as A_{vac} ,

$$\begin{aligned}
A_{\text{tot}}[n(r), e] = & A_{\text{vac}}[n(r)] \\
& + \frac{1}{2} \int \phi(\rho_s + \rho_b) - \frac{1}{2} \int \phi_h \rho_s \\
& + A_{\text{dm}}[n(r), e] + A_{\text{cav}}[n(r)]
\end{aligned}$$

The first order variation of the above functional with respect to the electronic charge density, $n(r)$, yields the Kohn-Sham potential

$$\begin{aligned}
\frac{\partial A_{\text{tot}}[n(r), e]}{\partial n} = & \frac{\partial A_{\text{vac}}[n(r)]}{\partial n} + \phi \frac{\partial \rho_b}{\partial n} + \phi - \phi_h \\
& + \frac{\partial A_{\text{dm}}[n(r), e]}{\partial n} \\
& + \frac{\partial A_{\text{cav}}[n(r)]}{\partial n}
\end{aligned}$$

Taking the first order variation of A_{tot} with respect to the non-dimensional electric field, e , and setting that to zero yields

$$e(1 - \alpha f(e)) = \frac{p_{\text{mol}} E}{kT} \quad (4.2)$$

where $E = -\nabla\phi$ is the electric field and the electrostatic potential ϕ is given by

$$\phi(r) = \int \frac{(\rho_b(r') + \rho_s(r'))}{|r - r'|} d^3 r', \quad (4.3)$$

The above equations along with the Kohn-Sham equation need to be solved simultaneously to obtain the ground state.

To put the above model into a more numerically amenable form, the following rearrangement is done.

Substituting for e in terms of E , the expression for polarization density becomes

$$\begin{aligned} P &= S(n(r))Np(f(e) + X(1 - \alpha f(e)))e \\ &= S(n(r))Np\left(\frac{f(e)}{(1 - \alpha f(e))} + X\right)\frac{p_{\text{mol}}E}{kT} \end{aligned}$$

Plugging in the above expression to the equation that relates dielectric displacement, D , with polarization density, P and rearranging it gives

$$\begin{aligned} D &= E + 4\pi P \\ &= E\left(1 + 4\pi S(n(r))\frac{Np^2}{kT}\left(\frac{f(e)}{(1 - \alpha f(e))} + X\right)\right) \\ &= \epsilon E \end{aligned}$$

where

$$\epsilon = 1 + 4\pi S(n(r))\frac{Np^2}{kT}\left(\frac{f(e)}{(1 - \alpha f(e))} + X\right), \quad (4.4)$$

the effective nonlinear relative permittivity of the solvent.

Applying the Maxwell equation that relates dielectric displacement to the free charge we get

$$\nabla \cdot \epsilon E = 4\pi(\rho_s), \quad (4.5)$$

a Poisson equation with a nonlinear dielectric constant that depends of $n(r)$ as well as the non-dimensional electric field e . In the equation ρ_s is the net charge density of the solute system.

Minimization with ionic contribution

The extra energy terms in A_{tot} due to the ions contribute the following additional terms to the Kohn-Sham potential on minimization with respect to $n(r)$

$$\phi \frac{\partial \rho_{\text{ion}}}{\partial n} + \frac{\partial A_{\text{ion}}[n(r), \eta_i]}{\partial n}$$

where the potential ϕ is given by

$$\phi(r) = \int \frac{(\rho_b(r') + \rho_s(r') + \rho_{\text{ion}}(r'))}{|r - r'|} d^3 r', \quad (4.6)$$

Taking the first order variation of A_{tot} with respect to the local ionic density field, $\eta_i(r)$, and setting that to zero yields

$$\eta_i(r) = \exp \left[-\frac{Z_i}{kT} \phi(r) - N_{\text{tot}} V_i \frac{2(x(r) - x_0)}{x_0(1 - x_0)(1 - x(r))^3} \right]$$

Thus the packing fraction, $x(r)$, becomes

$$x(r) = \sum N_i V_i \eta_i(r) \quad (4.7)$$

$$= \sum N_i V_i \exp \left[-\frac{Z_i}{kT} \phi(r) - N_{\text{tot}} V_i \frac{2(x(r) - x_0)}{x_0(1 - x_0)(1 - x(r))^3} \right] \quad (4.8)$$

and the Poisson equation becomes

$$\nabla \cdot \epsilon E = 4\pi(\rho_s + \rho_{\text{ion}}), \quad (4.9)$$

where ρ_s is the net charge density of the solute system and ρ_{ion} is the ionic charge density in the electrolyte given by $\rho_{\text{ion}} = s(r) \sum_i N_i Z_i \eta_i(r)$.

For a self-consistent solution, in each iteration the modified Kohn-Sham Hamiltonian need to be diagonalized simultaneously with the solutions to the above nonlinear Poisson equation and the accompanying transcendental equations.

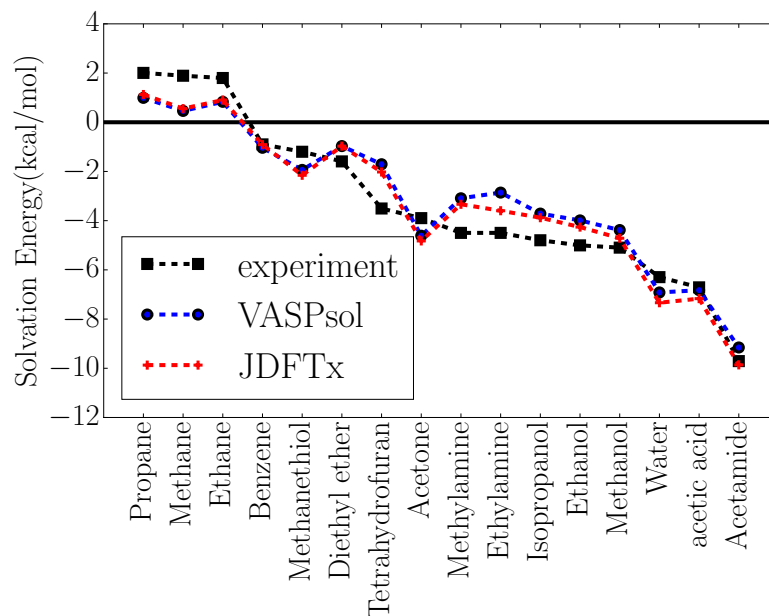


Figure 4.2: Comparison between the computed, the experimental and jdfdx solvation energies

4.4 Implementation and validation

The model described above is implemented in the massively parallel DFT code Vienna Ab-initio Software Package (VASP) [56, 77]. VASP is a plane-wave DFT code that makes use of the efficient fast Fourier transformations (FFT) to solve the Kohn-Sham Hamiltonian with periodic boundary conditions. The main changes required to incorporate the above model in VASP is the self-consistent update of the local potential in the Kohn-Sham Hamiltonian and the corrections to total free energy.

The crux of the implementation is in the solving of the nonlinear generalized Poisson equation described above. Apart from spatial dependency, the effective relative permittivity in the equation depends also on the non-dimensional field, e which is determined by the solution to the transcendental equation involving

the electric field E . For computational efficiency, the transcendental equation is solved at the beginning of the calculations for a range of values of the electric field and the results i.e values of ϵ stored in a lookup table. For any value of electric field that falls with the range but does not correspond to a value of electric field for which solution is available, spline fit is used to extrapolate the values. A self-consistent pre-conditioned Conjugate Gradient algorithm is used to solve the nonlinear generalized Poisson equation. The self-consistency requirement arises from the fact that the relative permittivity itself a functional of the non-dimensional field.

To benchmark and validate our implementation, first we compare the VASP-sol computed solvation energies of organic molecules against the experimental as well as values computed using JDFTx [95]. We also compare the surface energy of LiF 100 surface against the value obtained from a similar implementation in the DFT software package JDFTx. The VASPsol calculations were carried out with the projected augmented wave (PAW) [18] formalism describing the electron-ion interactions and the exchange-correlation effects accounted by the PBE [77] functional. For the surface calculations, the k-points required for the Brillouin zone integration were generated using the Monkhorst-Pack scheme with $8 \times 8 \times 1$ k-point mesh. For molecular and LiF 100 surface calculation, a plane wave basis set cutoff of 800eV was used. For BeO and MgO slabs a cutoff of 600 eV was used. For the solvent parameters we used the value from the reference [41]

Figure 4.2 compares the VASPsol computed solvation energies of organic molecules against the experimental values and the values obtained form JDFTx. As evident from the figure the agreement is very good. Next, we compare the

Table 4.1: Solvation energies of LiF (100) in units of eV per surface LiF unit

Solvent	E_{VASPsol}	E_{JDFTx}
Ethylene Carbonate	-0.08	-0.07
Propylene Carbonate	-0.08	-0.07

solvation energies of LiF 100 surface . LiF is chosen because of its highly ionic surfaces. Table 4.1 tabulates the surface energies of LiF 100 surface in Ethylene carbonate and Propylene carbonate solvents. The VASPsol values agrees pretty well with the JDFTx values.

4.5 Applications

Having benchmarked the model, it is applied to study how much of an effect non-linearity has on the solvent effects on alkaline earth metal oxides. Alkaline earth metal oxides are highly ionic with charges of +2 and -2 on the metallic species and the oxygen. More specifically we look at MgO and BeO. Table 4.2 lists the surface energies of various facets of MgO and BeO in water, Ethylene carbonate (EC) and Propylene Carbonate (PC). From the table it can be seen that for highly ionic systems like BeO the linear solvation model yield highly unphysical values for the surface energies which the nonlinear model is able to rectify.

Table 4.2: Surface energies of MgO and BeO slabs in units of eV/nm²

System	hkl	E_{vacuum}	$E_{\text{H}_2\text{O}}$	linear		nonlinear		
				E_{EC}	E_{PC}	$E_{\text{H}_2\text{O}}$	E_{EC}	E_{PC}
MgO	100	5.58	3.95	3.86	4.09	4.72	4.72	4.80
	110	13.56	9.34	9.16	9.61	11.52	11.53	11.73
	111	33.35	29.07	28.70	29.58	31.30	31.32	31.61
BeO	110	8.71	-9.51	-10.34	-8.31	7.96	7.96	8.03

4.6 Conclusions

implicit solvation model provides an efficient means to capture the solvent effects on a variety of systems. Typical solvation models approximate the polarization induced in the dielectric medium to be proportional to the the electric field. Though the linear models have been applied successfully to account for various experimentally observed solvent phenomena, it performs poorly when it comes to highly polar surfaces. In this work we describe a self-consistent nonlinear solvation model that accounts for the high electric field phenomenon known as the dielectric saturation. The model is implemented in the widely used DFT code VASP and the implementation is made available as a free and open-source module, VASPsol. The model and the implementation are benchmarked by comparing the computed values against corresponding experimental as well as other previously reported computed values. The benchmarked model was later employed to demonstrate its usefulness by applying to highly ionic surfaces of alkaline earth metal oxides. The nonlinear model corrects for the unphysical effects obtained by the linear model.

CHAPTER 5

HIGH-THROUGHPUT SCREENING OF INTERFACES ¹

5.1 Abstract

A Materials Project based open-source python tool, *MPInterfaces*, has been developed to automate the high-throughput computational screening and study of interfacial systems. The framework encompasses creation and manipulation of interface structures for solid/solid hetero-structures, solid/implicit solvents systems, nanoparticle/ligands systems ; and the creation of simple batch system agnostic workflows for in depth computational analysis using density functional theory or molecular dynamics. In this work we describe various algorithms and methods implemented in the package. Using several test cases we demonstrate how the package leverages the already existing open-source high-throughput tools and extends their capabilities towards the understanding of interfacial systems. The package enables high-throughput computational screening of advanced materials, directly contributing to the Materials Genome Initiative (MGI), which aims to discover, develop, and deploy new materials twice as fast as currently possible.

5.2 Introduction

Interfaces play a vital role in practically all materials and devices [49, 74, 16, 42]. For instance, the efficiency and stability of electrochemical devices are mostly

¹To be published as 'Kiran Mathew, A. Singh, J. Gabriel, F. Tavazza, A. Davydov and R. G. Hennig, *MPInterfaces: A Materials Project based python tool for a high throughput computational screening of interfacial systems*'

decided by the composition and the properties of the Solid electrolyte interface (SEI) layers [65]. In another example, the self assembly of nanoparticles used in high-efficiency photo-voltaic devices is directed by the interface formed between nanoparticles, ligands and the solvent they are dispersed in [13, 14]. As materials and devices are getting smaller, the interface properties begin to dominate their essential characteristics. Progress in a wide variety of applications ranging from catalysis to microelectronics is guided by a refinement of our understanding and control of the interface properties.

Experimental studies combined with computational investigations provide a broad spectrum of information needed for an accurate and thorough understanding of interfaces, which is seldom accessible by utilizing one of these two approaches alone. Moreover, experimental screening of a large number of possible candidate systems poses a daunting challenge due to time-consuming and expensive experiments, besides limitations involved while exploring extreme and hazardous environmental conditions. In order to complement and guide experimental investigation, and to accelerate the discovery of novel phenomenon at interfaces it is imperative to adopt a rational approach towards the screening and the characterization of interfacial systems. The advancement of modern computing has pushed the boundaries of computation making them faster, cost-effective, efficient and accurate. The first examples of the use of computational methods to screen for new materials is being seen increasingly [93, 23, 7, 40, 4, 39].

Interfaces are more difficult to investigate than other aspects of materials' properties due to the large number of configurations and conformations possible in these two (or more) phase systems. To enable the high-throughput

screening of thermodynamically stable nanoparticle-ligand-solvent interfaces, nanoparticle shapes and two-dimensional (2D) material-substrate interfaces we have developed the open-source python package, *MPInterfaces*. In addition to the various interfacial structure generation, this package automates preparation of input files to first principles density-functional theory (DFT) simulations softwares like Vienna Ab-initio Software Package (VASP) [56] and molecular dynamics (MD) simulations softwares like Large-scale Atomic/Molecular Massively Parallel Simulator (LAMMPS) [80]. It also enables the creation of computational workflows that can be deployed on remote computing resources. The coupling with the energy calculation softwares and the workflow creation builds on the framework of the open source python packages of the Materials Project namely pymatgen [73], custodian [73] and fireworks [48].

The package is being continuously developed and the latest version can be obtained from the GitHub repo at <https://github.com/henniggroup/MPInterfaces>. In the following sections we present an overview of the package using examples, where relevant; describing its capabilities and discussing algorithms which were used to overcome some of the formidable technical and scientific hurdles.

5.3 *MPInterfaces*: Overview with examples

The *MPInterfaces* package is written in Python2.7 with support for Python3.x. The package makes extensive use of existing Python tools for the generation and manipulation of various interfacial structures as well as input files for various DFT/MD softwares. For structural analysis and input file generation we extend the pymatgen package, with the Atomic Simulation Environment [10] package

used to fill in the gaps. For workflow creation and management we extend the custodian and the fireworks packages. In the following subsections we discuss the capabilities supported by the *MPInterfaces* package that are built on top of the aforementioned packages. Illustrative examples with corresponding code snippets are also provided along with each section to further drive the message home.

5.3.1 Ligand capped nanoparticles

Nanocrystals in the form of quantum dots are used increasingly in the fabrication of devices such as solar cells, transistors, and LEDs [27, 19]. Often assembly of such nanocrystals into superlattices yields new materials with tunable optical and electronic properties [13, 14]. DFT calculations and MD simulations are routinely used to characterize interfaces properties that are hard to access with stand alone experiments; for example, binding energies and surface energy changes in varying environments of capping ligand and solvents [24, 14].

It is well known that nanocrystal surface chemistry as well their shape evolution are controlled by the thermodynamics and kinetics of the three phase system comprising the nanoparticle, surfactant molecules (known as capping ligands) and the solvents [24]. Further, the energetics of the system determine thermodynamic and kinetic barriers to the growth of such nanoparticles, which drives their size, shape and properties.

MPInterfaces enables a high-throughput computational screening of nanoparticle/ligand combinations by varying the following degrees of freedom in the system: (a) crystallographic planes or facets,(b) ligand binding sites

on each facets and (c) the ligand surface coverage for the given facet-ligand-binding site combinations.

Treating these interfaces as a crystallographic facet slab model of a specified thickness with an adsorbate ligand on the surface, we construct these interfaces by specifying the following inputs: (a) the bulk phase that constitutes the surface in question, (b) the crystallographic facet of interest in this bulk phase, (c) the initial binding site on the surface, (d) the binding atom on the ligand that is intuitively expected to be the nearest neighbor to the chosen binding site on the surface, (e) the initial approximate separation between the surface binding site and the atom, which in other words is the adsorption distance and (f) a specified coverage of the surface calculated in number of ligands per unit area.

Figure 5.1 demonstrates the degrees of freedom that can be controlled for an interface model of (100) surface of PbS and lead acetate, $\text{Pb}(\text{CH}_3\text{COO})_2$, ligands. The *interfaces.py* module in the package also defines the python classes for the creation of ligands from the combinations of different molecules. The molecule structures can be generated using the python interface to openbabel [72] or can be directly read in from the already available structure files of various format supported by pymatgen. The ligands are then adsorbed on a slab of specified (*hkl*) miller index and surface coverage and with a variability in configurations on the surface, as illustrated in Figure 5.1. Additionally a liquid phase, a solvent, can be added to the nanoparticle-ligand interface in an efficient and accurate manner by using implicit solvent models coupled with DFT, for instance the linear and non-linear solvent models recently implemented into the VASP code like VASPsol [68].

A code excerpt for generation of a single

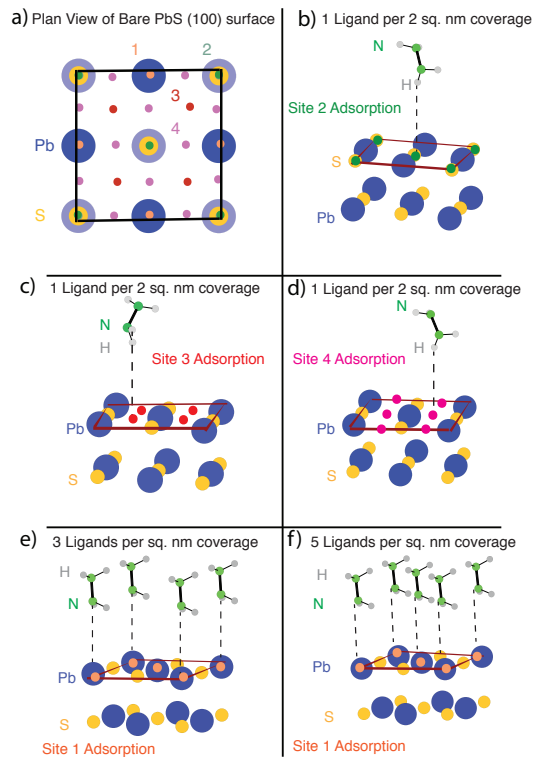


Figure 5.1: (a) Top view of a rocksalt (100) surface of Lead Sulfide (PbS) denoted as PbS(100). High symmetry binding sites 1,2,3,4 on this facet are marked as orange, green, purple and red respectively. Lead (Pb) is indicated in blue and Sulfur (S) in yellow. Hydrazine ligand placed on (b) site 2, above an S atom on of PbS(100) bound through the Nitrogen (N - Green) atom on the ligand, (c) site 3 of PbS(100) referenced with adsorption distance bound through the Hydrogen (H - Grey) atom on the ligand, (d) site 4 of PbS(100) bound through the N atom on the ligand with a random rotation about cartesian axes, (e) higher coverage on site 1 above a Pb atom, binding through N atom, (f) a high coverage over site 4, binding through N atom. Notice the preservation of symmetry between the molecules to minimize the steric hindrance. Other entropic configurations can be included with manual manipulation of binding sites. We calculate the interfacial property of binding energy per ligand.

nanoparticle facet-ligand interface

All distances are in Angstroms

```

from mpinterfaces.interface import Ligand, \
                                Interface

Bulk_struct = Structure.from_file("POSCAR.bulk")
hkl = [1,0,0]
min_thick = 10
min_vac = 30
# ligands per sq. Angstroms
surface_coverage = 0.03
hydrazine = Molecule.from_file(
                                "hydrazine.xyz")
ligand= Ligand([hydrazine])
# position the ligand
x_shift = 1.5
y_shift = 1.5
z_shift = 1.5
adsorb_on_species = ['Pb','S']
adatom_on_ligand=['N','H']
interface = Interface(
    bulk_struct, hkl=hkl,
    min_thick=min_thick,
    min_vac=min_vac,
    ligand=ligand,
    displacement=z_shift,
    x_shift=x_shift, y_shift = y_shift
    adatom_on_lig=adatom_on_ligand,
    adsorb_on_species= adsorb_on_species,
    surface_coverage=surface_coverage)
interface.create_interface()

```

5.3.2 Wulff construction

As mentioned before, nanocrystal shapes as well as their super cell self-assemblies depend strongly on the thermodynamics and kinetics of the system comprising of the nanoparticles, ligands and the solvent. For surface capped with ligands, the surface energy, γ_{hkl} , as a function of the ligand coverage is given by [14]

$$\gamma_{hkl} = \gamma_{hkl}^0 + \Theta_{hkl} E_{b,hkl}$$

where γ_{hkl}^0 is the bare slab surface energy, Θ_{hkl} is the surface coverage and $E_{b,hkl}$ is the binding energy of the ligand. Given the surface energies of all facets of interest in the crystal structure, it is possible to predict the effective shape of a nanocrystal using the Wulff construction [50]. Based on the Wulff theorem [44], Wulff construction in its simplest form states that a nanocrystal assumes a multifaceted shape which minimizes its net surface energy. In comparison to the Wulff construction supported by the ASE package, which supports only cubic crystal systems, our implementation can handle arbitrary crystal systems as we employ pymatgen for the analysis of various crystallographic facets.

The *nanoparticle.py* module in the *MPInterfaces* package implements the classes that lets the user provide the list of miller index families, their corresponding surface energies and the maximum radius of the nanoparticle and create the nanocrystal according to the Wulff construction.

```
# A code excerpt for generation of  
# PbS nanoparticle
```

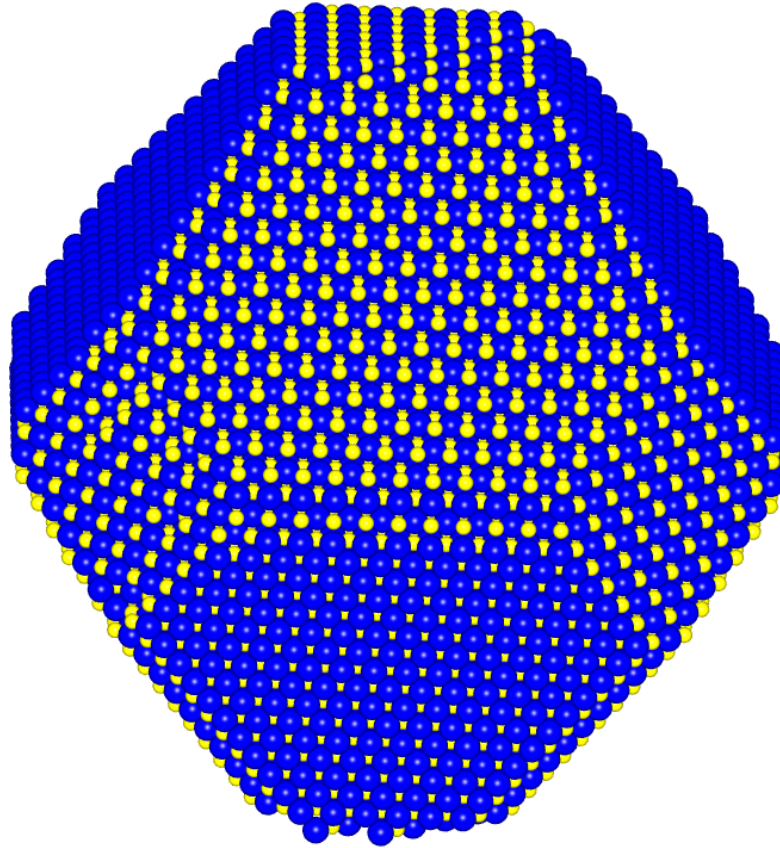


Figure 5.2: The shape of a PbS nanocrystal generated using the Wulff construction supported by *MPInterfaces*. The code snippet used for the creation of nanoparticle is provided. The surface energies are from the reference [68].

```
# All distances are in Angstroms and  
# surface energies in meV per square  
# Angstroms  
  
from mpinterfaces.nanoparticle import \  
    Nanoparticle  
  
rmax = 50  
hkl_family = [(1,1,1), (1,1,0)]  
surface_energies = [24, 28]
```

```
nanoparticle = Nanoparticle(  
    bulk_structure,  
    rmax=rmax,  
    hkl_family=hkl_family,  
    surface_energies=surface_energies)  
nanoparticle.create()
```

5.3.3 Heterostructure interfaces

The first step in the study of hetero-junctions of solid-state materials' is the creation of interfaces between any two crystal structures, which is a very challenging task. This is due to the fact that there exists numerous possible Coincident Site Lattices (CSL) [86, 46] that can be used to create these hetero-structures interfaces. Moreover, additional possibilities arise due to all the possible placement of atoms at the interface. A very simplistic approach would be to do a brute force search of the coincidence lattice vectors between two surfaces, however this is not only inefficient but is also inapplicable for surfaces with different crystal symmetry. [46]

In this package we have developed an algorithm which rapidly scans through various surface configurations of an interface between two crystal surfaces and identifies those pairs which are within a specified lattice-mismatch, are symmetry-matched and distinct from each other. The efficient lattice matching algorithm proposed by Zur *et al.* [107], described in Figure 5.3, is used to find the lattice-matched and symmetry-matched interfaces of any two surfaces for all rotations. The number of possible CSLs in this algorithm depends on the

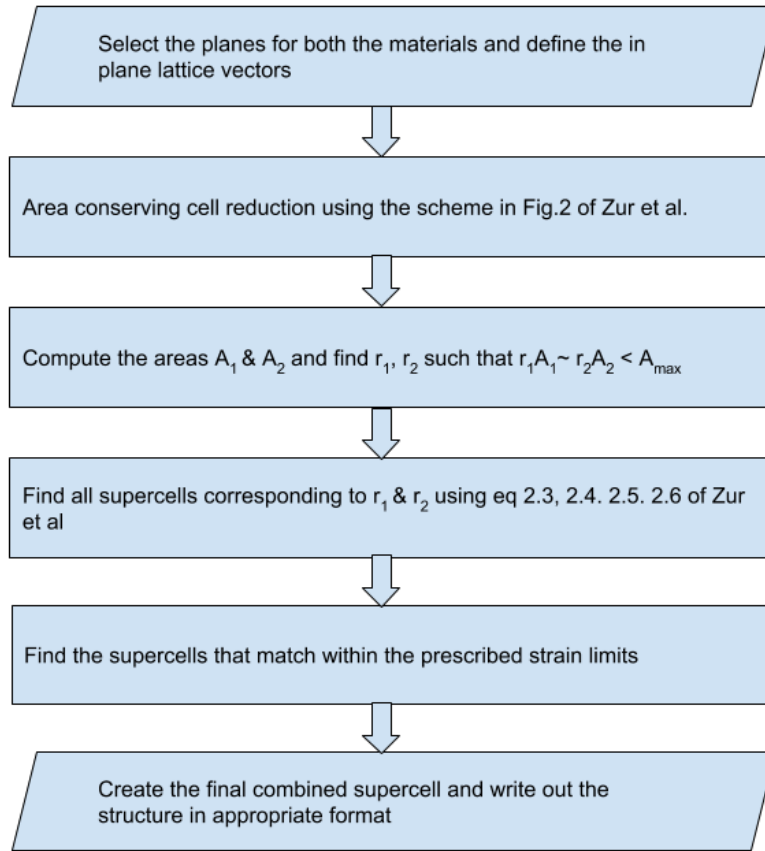


Figure 5.3: The algorithm of Zur *et al.* [107] for the epitaxial lattice-matching and symmetry-matching of any two surfaces for all rotations; within a given lattice mismatch and within a given surface area of the interface.

maximum permitted interface area and the maximum lattice-mismatch that the interface is allowed to undergo. The surface matching of the interface atoms is performed by identifying the distinct atoms in the near-interface layers and creating all distinct structures formed by placing the non-distinct atoms on top of each other.

Combined with the input file generation and workflow management features of *MPInterfaces*, this algorithm can be used to perform high-throughput computational screening of suitable substrates for 2D material deposition and functionalization. [92] Given a list of 2D materials and substrates, using the *MP-*

	a	$\epsilon_{1:1}$	ϵ_{MP}	S_{sub}	S_{gr}
Graphene	2.46				
Pt	3.98	12.55	0.98	$\sqrt{3} \times \sqrt{3}$	2×2
Cu	3.62	3.92	-3.92	1×1	1×1
Au	4.17	16.45	-3.53	$\sqrt{3} \times \sqrt{3}$	2×2
Pd	3.95	11.71	1.94	$\sqrt{3} \times \sqrt{3}$	2×2
Ni	3.52	0.93	-0.93	1×1	1×1
Al	4.07	14.37	-1.12	$\sqrt{3} \times \sqrt{3}$	2×2
Ag	4.14	15.82	-2.79	$\sqrt{3} \times \sqrt{3}$	2×2

Table 5.1: The lattice parameter, a (Å), of graphene and (111) surfaces of Pt, Cu, Au, Pt, Ni, Al and Ag is shown in the table. The lattice-mismatch between the primitive lattices of graphene and substrate, $\epsilon_{1:1}$ in (%), is compared with the lattice-mismatches obtained from *MPInterfaces* code, ϵ_{MP} (%). The supercells of substrate, S_{sub} , and graphene, S_{gr} , obtained from *MPInterfaces* are listed as well.

Interfaces package we find the CSLs for each substrate/2D material pair and subsequently generate the structure files for the combined structure for further DFT or MD analysis. A study of the thermodynamics of the system and effects of substrate on the 2D material properties can reveal if the growth of a particular 2D materials is feasible on that substrate; and if the substrate alters any of the 2D materials properties [92, 91, 94, 90, 106].

Graphene has a hexagonal lattice with a lattice parameter of 2.46 Å. Table 5.4 lists the lattice-mismatch between graphene and 7 potential substrates, the (111) surfaces of Pt, Pd, Cu, Ag, Ni, Au and Al. A 1:1 match of graphene-substrate primitive cells results in lattice-mismatches, $\epsilon_{1:1}$, exceeding 10%, except for Cu and Ni. *MPInterfaces* identifies that a $\sqrt{3} \times \sqrt{3}$ supercell of all the other metal (111) surfaces is matched with the 2×2 surface of graphene within a lattice mismatch, ϵ_{MP} , of $< 4\%$. Figure 5.4 shows a schematic of the interfaces obtained for graphene and the 7 substrates.

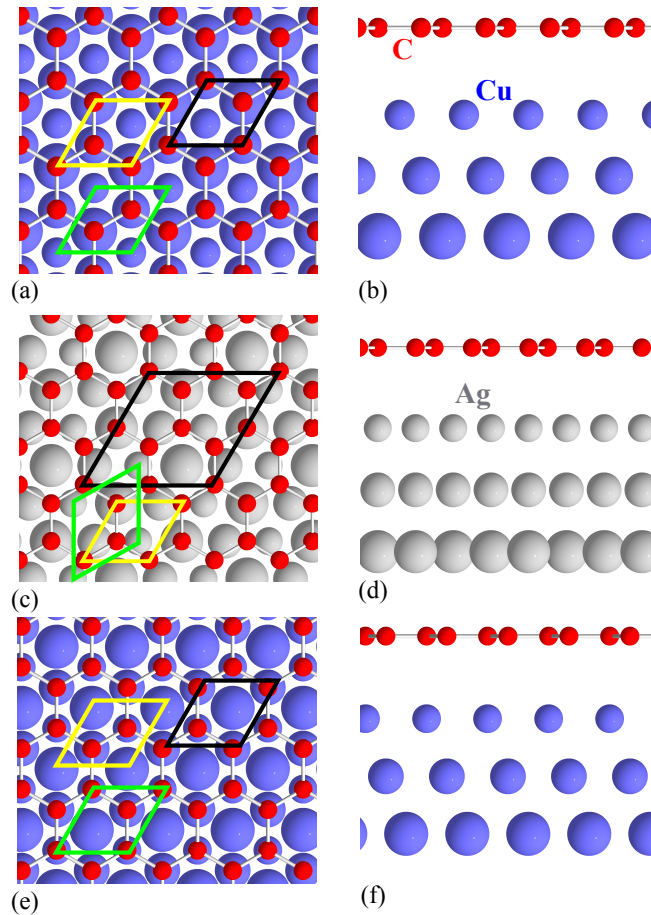


Figure 5.4: (a) Top view and (b) side view of 1:1 match between strained graphene and Ni(111) (or Cu(111)). (c) Top view and (d) side view of 2×2 graphene strained by $< 4\%$ to match the $\sqrt{3} \times \sqrt{3}$ supercells of Pt(111) (or Pd(111), Ag(111), Au(111) and Al(111)) surfaces. The primitive cell of graphene is shown with a yellow box, that of the substrates with a green box, and lattice-matched cells of graphene and substrates with a black box. Another configuration for (a) is shown in (e) top view and (f) side view, but with a different surface placement of the atoms at the interface. The substrate atoms beyond the third layer from the interface are hidden for clarity.

```

# A code excerpt for generation of interfaces
# between graphene and substrates
# within a give lattice mismatch and maximum

```

```

# area of the interface surface
# All distances are in Angstroms and lattice
# mismatches in percent

from mpinterfaces.interface import Interface
from mpinterfaces.transformations import *
from mpinterfaces.utils import *

separation = 3
nlayers_2d = 2
nlayers_substrate = 2
# Lattice matching algorithm parameters
max_area = 400
max_mismatch = 4
max_angle_diff = 1
r1r2_tol = 0.01

substrate_bulk = Structure.from_file(
    'POSCAR_substrate')
substrate_slab = Interface(substrate_bulk,
    hkl = [1,1,1],
    min_thick = 10,
    min_vac = 25,
    primitive = False,
    from_ase = True)
mat2d_slab = slab_from_file([0,0,1],
    'POSCAR_2D')

# get aligned lattices
substrate_slab_aligned, mat2d_slab_aligned =

```

```
get_aligned_lattices(  
    substrate_slab,  
    mat2d_slab,  
    max_area = max_area,  
    max_mismatch = max_mismatch,  
    max_angle_diff = max_angle_diff,  
    rlr2_tol = rlr2_tol)  
  
# merge substrate and mat2d in all possible  
# ways  
  
hetero_interfaces = generate_all_configs(  
    mat2d_slab_aligned,  
    substrate_slab_aligned,  
    nlayers_2d,  
    nlayers_substrate,  
    separation
```

5.3.4 Workflows

Any computational analysis of a materials system involves an initial setup of a computational model (generation of the interface models as described in previous sections), a series of calculations which may depend on each other and optional automated post processing of the computed data into presentable information. This constitutes a computational workflow. The package supports the writing of simplified computational workflows where each step is a simple python function that can take in as arguments the values returned by the function in the preceding step.

The computational job management and workflow creation extends the Materials Project packages *Custodian* [73] and *Fireworks* [48]. In comparison to the Fireworks workflows that links together objects of Fireworks class in Direct Acyclic Graph (DAG), our workflows constitute simple linearly connected jobs described by python functions. A major difference between this workflow and that of Fireworks is that we do not use a database for the archiving and launching of workflows; this design aspect of Fireworks enables fetching of the workflows from a remote database when in need and the subsequent launching of jobs in the workflow on the cluster. We built on these workflow ideas, and developed a simple and portable workflow creation and job management system, that manages computational high throughput discovery projects run on differing job queue systems like SLURM and PBS.

Our workflows are typically a combination of sequences of structure input and manipulation, and the calculation of the energy or a material property of the structure, and post processing of calculated data to extract required information. Each workflow is divided into steps, which can be any part of the aforementioned sequence. Jobs are managed on computational queue systems with JSON formatted checkpoint files as previously described. Our workflow design employs simple Java Serializable Object Notation (JSON) checkpoint files for keeping track of the jobs and their completion status on the queue. This enables comprehensive logging of errors and for specific error handling measures to be taken. This provides a concise logging of the energies calculated for each calculation in a single file together with information on input files and parameters used for each calculation in the workflow. These features aid source of error analysis and direct a specific application of error handling corrections to specific jobs, where we could not apply generalized auto-correction schemes.

This has especially been found useful in handling queue errors, which can be as high as 10% on large supercomputing clusters. We adopted this simplified implementation because we did not have the administrative privilege to setup up a dedicated workflow database on each individual computational resource that we have access to. This also simplifies the setting up of the workflow environment on arbitrary computing resources. We note and highlight that the job management system caters to the loads of general investor queues on large supercomputer clusters like HiPerGator and the XSEDE resources of Stampede which use the PBS and SLURM job scheduling systems respectively. In addition, partition batch jobs management implemented in this high throughput materials analysis framework facilitates a controlled load on the job scheduler.

5.4 Conclusions

We have implemented a materials project based open-source python package, *MPInterfaces*, that extends the capabilities of the existing high-throughput frameworks such as pymatgen, custodian and fireworks, towards the study of interfacial systems. The package is being continuously developed and is hosted on GitHub <https://github.com/henniggroup/MPInterfaces>. We demonstrate the usefulness of the package and its capabilities by various illustrative examples accompanied by their corresponding code snippets. By avoiding reinventing the wheel through the use of existing efficient tools, with this open-source undertaking, we intent to provide a collaborative platform that welcomes any interested user to review and improve the code base and help push the limits of state of the art computational modeling of interfaces.

CHAPTER 6

CONCLUSIONS

Proper understanding of interfaces – solid/solid and solid/liquid – requires an appropriate mix of experimental and computational techniques. Computing has grown cheaper and powerful over the years. In order to properly exploit these computational resources so as to shed more light on the experimental observations we need better computational methodologies and efficient tools. In this thesis we developed (i) a hierarchy of methods for the *ab-initio* description of solid/liquid interfaces using implicit solvation models with increasingly detailed description of the liquid and (ii) a high-throughput framework for the rapid setup, calculation, and analysis of solid/solid and solid/liquid interfaces.

First principles approaches provide a very accurate means to understand the complete electronic structure of arbitrary systems. Solving full N -electron Schrödinger's equation for systems that are not hydrogen is impossible even with the best available computational resources. Proper approximations that form a compromise between accuracy and efficiency are needed. Density functional theory is one such approximation that reduces the cost significantly without sacrificing the accuracy. It is built upon the principle that the energy of the system can be written as a functional of the electronic charge density. Typical DFT implementations and use cases are focused more towards solid state systems. Explicit treatment of liquids in DFT poses a serious challenge due to the large number of degree of freedoms involved and the requirement of statistical sampling. Treating the solvent effects on the solute implicitly offers an efficient means to describe solid/liquid interfaces. The work described in this thesis has been focused mostly on the implementation of various implicit solvation mod-

els in the self-consistent DFT framework as implemented in the widely used plane wave DFT code VASP and its subsequent application to technologically important solid/liquid interfaces.

Chapter 2 described the self-consistent implementation of the linear implicit solvation model. In this polarizable continuum model, set in the rigorous framework of JDFT, the solute is immersed in a dielectric medium that describes the solvent. The polarization induced in the medium is assumed to be proportional to the electric field. Also the relative permittivity is a functional of the electronic charge density of the solute so that its values varies smoothly from vacuum value in the bulk of the solute to the solvent bulk value far away from the solute. The linear model proved to be very useful and efficient in accounting for the solvent effects on metallic and semiconductor surfaces as well as the reaction energy barriers in solvent.

Chapter 3 described the extension of the linear model to include the screening effect due to the ions in the solution in addition to the dielectric screening. This in effect models an electrolyte with the ionic charge density in the solvent modulated by the Boltzmann distribution. For small potential the ionic charge density can be linearized and yields the Poisson-Boltzmann equation for the electrostatic potential in the system. This model proved to be useful in capturing the diffuse double layer formed at the electrode/electrolyte interface and in enabling the modeling of electrochemical cell at an ab-initio level.

Though the linear models provide an efficient means to account for solvent effects, it fares poorly for systems such as ionic surfaces where large electric fields are present at the interface. For such systems applying linear model yields unphysical results such as negative surface energies. The linear model also fails

to account for the finite size of the ions in the solvent. This, for systems with large electric field, could lead to unphysical charge build up at the interface. In Chapter 4 we described model extensions that account for the high field phenomenon such as the dielectric saturation and the finite size of the ions.

The solvation models, reworked into the self-consistency framework, are implemented in the widely used DFT software VASP. The open-source modules are made freely available on the public code hosting website *github*. The implementation has been used extensively by other researchers to study the solvent effects of various phenomena and the module is now part of the official VASP source code.

Outlook for VASPsol. The self-consistent solvation model framework implemented in VASP is based on modifications of the electrostatic description and the local Kohn-Sham potential. The generality of this implementation can be leveraged to incorporate advanced solvation models in VASP, either by direct implementation in VASP or by linking it with external libraries such as the JDFT library.

Chapter 5 described the development and implementation of a software framework for the rapid screening of interfaces in order to accelerate the discovery of novel materials. The open source framework written in the python programming language extends already existing well tested frameworks to enable high-throughput screening of various interfaces such as: solid/liquid, nanocrystal/ligands and heterostructure interfaces. The framework enables generation of all possible interface structures and input files for various software tools for rapid screening as well as an in depth analysis of each generated structure.

Outlook for MPIInterfaces. The *MPIInterfaces* package is continuously being developed and the current implementation enables one to easily extend the framework's capabilities to include new and exciting features. Features such as the generation of grain boundaries for arbitrary tilt and twist angles can be incorporated without any significant efforts. Other features such as efficient surrogate models for screening the interfaces that are either pre-parameterized like empirical potentials or learned on the fly such as machine-learning methods can significantly accelerate the materials discovery by weeding out unfit structures before being screened by the expensive DFT and MD tools.

Apart from developing methodologies and algorithms, significant effort has been spent as part of this work to ensure practical applicability of the methods developed. This involved implementing the models in the widely used legacy DFT code VASP. Working with legacy codes is often hampered by poor documentation and the usage of outdated software engineering models that arises from the fact that the software development has evolved considerably since the first release of the code. Often ignored in computational method development is the need for adopting better software development practices to ensure quick delivery of efficient and transparent code. These challenges have served a major motivation for shifting the development of newer tools such as the high-throughput screening framework *MPIInterfaces* to a more open-source collaborative platforms using modern programming languages and software development techniques. This has helped immensely in ensuring a maintainable code base with minimal transition time for newer contributors.

BIBLIOGRAPHY

- [1] [https://en.wikipedia.org/wiki/Double_layer_\(interfacial\)](https://en.wikipedia.org/wiki/Double_layer_(interfacial)).
- [2] Victor A. Agubra and Jeffrey W. Fergus. The formation and stability of the solid electrolyte interface on the graphite anode. *Journal of Power Sources*, 268:153 – 162, 2014.
- [3] Marcel Aguilera-Arzo, Andreu Andrio, Vicente M Aguilera, and Antonio Alcaraz. Dielectric saturation of water in a membrane protein channel. *Physical chemistry chemical physics : PCCP*, 11(2):358–65, jan 2009.
- [4] Martin P Andersson, Thomas Bligaard, Arkady Kustov, Kasper E Larsen, Jeffrey Greeley, Tue Johannessen, Claus H Christensen, and Jens K Nørskov. Toward computational screening in heterogeneous catalysis: Pareto-optimal methanation catalysts. *Journal of Catalysis*, 239(2):501–506, 2006.
- [5] O. Andreussi, I. Dabo, and N. Marzari. *J. Chem. Phys*, 136:064102, 2012.
- [6] T. A. Arias, M. C. Payne, and J. D. Joannopoulos. *Phys. Rev. Lett*, 69:1077, 1992.
- [7] Rickard Armiento, Boris Kozinsky, Marco Fornari, and Gerbrand Ceder. Screening for high-performance piezoelectrics using high-throughput density functional theory. *Phys. Rev. B*, 84:014103, Jul 2011.
- [8] Pankaj Arora. Capacity Fade Mechanisms and Side Reactions in Lithium-Ion Batteries. *Journal of The Electrochemical Society*, 145(10):3647, 1998.
- [9] Daniel J. Asunskis, Igor L. Bolotin, and Luke Hanley. Nonlinear optical properties of pbs nanocrystals grown in polymer solutions. *J. Phys. Chem. C*, 112(26):9555–9558, 2008.
- [10] S. R. Bahn and K. W. Jacobsen. An object-oriented scripting interface to a legacy electronic structure code. *Comput. Sci. Eng.*, 4(3):56–66, May-Jun 2002.
- [11] William J. Baumgardner, Joshua J. Choi, Yee-Fun Lim, and Tobias Hanrath. Sns nanocrystals: Synthesis, structure, optical properties, and surface chemistry. *J. Am. Chem. Soc.*, 132(28):9519–9521, 2010.

- [12] William J. Baumgardner, Kevin Whitham, and Tobias Hanrath. Confined-but-connected quantum solids via controlled ligand displacement. *Nano Letters*, 13(7):3225–3231, 2013.
- [13] William J Baumgardner, Kevin Whitham, and Tobias Hanrath. Confined-but-Connected Quantum Solids via Controlled Ligand Displacement. *Nano letters*, jun 2013.
- [14] Clive R. Bealing, William J. Baumgardner, Joshua J. Choi, Tobias Hanrath, and Richard G. Hennig. Predicting nanocrystal shape through consideration of surface-ligand interactions. *ACS Nano*, 6(3):2118–2127, 2012.
- [15] Axel D Becke. Perspective: Fifty years of density-functional theory in chemical physics. *The Journal of chemical physics*, 140(18):18A301, may 2014.
- [16] Debasis Bera, Lei Qian, Teng-Kuan Tseng, and Paul H. Holloway. Quantum Dots and Their Multimodal Applications: A Review. *Materials*, 3(4):2260–2345, mar 2010.
- [17] Simon Billinge. Materials science: Nanoparticle structures served up on a tray. *Nature*, 495:453–454, 2013.
- [18] P. E. Blöchl. Projector augmented-wave method. *Phys. Rev. B*, 50:17953–17979, Dec 1994.
- [19] Werner Stober; Ernst Bohn. The renaissance of dye-sensitized solar cells. *Nature Photonics*, 6(3):162–169, feb 2012.
- [20] Kieron Burke and Lucas O. Wagner. DFT in a nutshell. *International Journal of Quantum Chemistry*, 113(2):96–101, jan 2013.
- [21] J Chazalviel. Electrochemical aspects of the generation of ramified metallic electrodeposits. *Physical review. A*, 42(12):7355–7367, dec 1990.
- [22] Jun Chen, Xingchen Ye, Soong Ju Oh, James M. Kikkawa, Cherie R. Kagan, and Christopher B. Murray. Bistable magnetoresistance switching in exchange-coupled $\text{CoFe}_2\text{O}_4/\text{Fe}_3\text{O}_4$ binary nanocrystal superlattices by self-assembly and thermal annealing. *ACS Nano*, 7(2):1478–1486, 2013.
- [23] Lei Cheng, Rajeev S. Assary, Xiaohui Qu, Anubhav Jain, Shyue Ping Ong, Nav Nidhi Rajput, Kristin Persson, and Larry A. Curtiss. Accelerating

electrolyte discovery for energy storage with high-throughput screening. *The Journal of Physical Chemistry Letters*, 6(2):283–291, 2015.

- [24] Joshua J. Choi, Clive R. Bealing, Kaifu Bian, Kevin J. Hughes, Wenyu Zhang, Detlef-M. Smilgies, Richard G. Hennig, James R. Engstrom, and Tobias Hanrath. Controlling nanocrystal superlattice symmetry and shape-anisotropic interactions through variable ligand surface coverage. *J. Am. Chem. Soc.*, 133(9):3131–3138, 2011.
- [25] Christopher J. Cramer and Donald G. Truhlar. A universal approach to solvation modeling. *Accounts of Chemical Research*, 41(6):760–768, 2008.
- [26] Rezan Demir-Cakan. Targeting the role of lithium sulphide formation for the rapid capacity fading in lithium-sulphur batteries. *Journal of Power Sources*, 282:437 – 443, 2015.
- [27] P. Dey, J. Paul, J. Bylsma, D. Karaiskaj, J.M. Luther, M.C. Beard, and a.H. Romero. Origin of the temperature dependence of the band gap of PbS and PbSe quantum dots. *Solid State Communications*, 165:49–54, jul 2013.
- [28] K. A. Dill, S. Bromberg, K. Yue, K. M. Fiebig, D. P Yee, P. D. Thomas, and H. S. Chan. Principles of protein folding—a perspective from simple exact models. *Protein Science: A Publication of the Protein Society*, 4(4):561602, 1995.
- [29] K a Dill, S Bromberg, K Yue, K M Fiebig, D P Yee, P D Thomas, and H S Chan. Principles of protein folding—a perspective from simple exact models. *Protein science : a publication of the Protein Society*, 4(4):561–602, 1995.
- [30] Bernd Ensing, Evert Jan Meijer, P. E. Blöchl, and Evert Jan Baerends. Solvation effects on the sn2 reaction between ch3cl and cl- in water. *J. Phys. Chem. A*, 105(13):3300–3310, 2001.
- [31] J. L. Fattebert and F. Gygi. *Int. J. Quantum Chem.*, 93:139, 2003.
- [32] P. J. Ferreira, G. J. la O, Y. Shao-Horn, D. Morgan, R. Makharia, S. Kocha, and H. A. Gasteiger. Instability of PtC Electrocatalysts in Proton Exchange Membrane Fuel Cells. *Journal of The Electrochemical Society*, 152(11):A2256, 2005.
- [33] Carlos Fiolhais. A Primer in Density Functional Theory. 620, jun 2003.

- [34] Matthew Fishman, Houlong L. Zhuang, Kiran Mathew, William Dirschka, and Richard G. Hennig. Accuracy of exchange–correlation functionals and effect of solvation on the surface energy of copper. *Phys. Rev. B*, 87:245402, Jun 2013.
- [35] James B. Foresman, Todd A. Keith, Kenneth B. Wiberg, John Snoonian, and Michael J. Frisch. Solvent effects. 5. influence of cavity shape, truncation of electrostatics, and electron correlation on ab initio reaction field calculations. *J. Phys. Chem.*, 100(40):16098–16104, 1996.
- [36] M. J. Frisch, G. W. Trucks, H. B. Schlegel, G. E. Scuseria, M. A. Robb, J. R. Cheeseman, G. Scalmani, V. Barone, B. Mennucci, G. A. Petersson, et al. Gaussian 09, revision a. 02, gaussian. *Inc., Wallingford, CT*, 270:271, 2009.
- [37] P. Giannozzi. *J. Phys.: Condens. Matter*, 21:395502, 2009.
- [38] X. Gonze, J.-M. Beuken, R. Caracas, F. Detraux, M. Fuchs, G.-M. Rignanese, L. Sindic, M. Verstraete, G. Zerah, F. Jollet, M. Torrent, A. Roy, M. Mikami, Ph. Ghosez, J.-Y. Raty, and D.C. Allan. First-principles computation of material properties: the abinit software project. *Comp. Mater. Sci.*, 25(3):478 – 492, 2002.
- [39] Jeff Greeley, Thomas F Jaramillo, Jacob Bonde, IB Chorkendorff, and Jens K Nørskov. Computational high-throughput screening of electrocatalytic materials for hydrogen evolution. *Nature materials*, 5(11):909–913, 2006.
- [40] Jeff Greeley and Jens K. Nørskov. Combinatorial density functional theory-based screening of surface alloys for the oxygen reduction reaction. *The Journal of Physical Chemistry C*, 113(12):4932–4939, 2009.
- [41] Deniz Gunceler, Kendra Letchworth-Weaver, Ravishankar Sundararaman, Kathleen A Schwarz, and T A Arias. The importance of nonlinear fluid response in joint density-functional theory studies of battery systems. *Modelling Simul. Mater. Sci. Eng.*, 21(7):074005, 2013.
- [42] Don-hyung Ha, Andrew H Caldwell, Matthew J Ward, Shreyas Honrao, Kiran Mathew, Robert Hovden, Margaret K a Koker, David a Muller, Richard G Hennig, and Richard D Robinson. Solid Solid Phase Transformations Induced through Cation Exchange and Strain in 2D Heterostructured Copper Sul fi de Nanocrystals. *Nano letters*, 2014.

- [43] Don-Hyung Ha, Mohammad A. Islam, and Richard D. Robinson. Binder-free and carbon-free nanoparticle batteries: A method for nanoparticle electrodes without polymeric binders or carbon black. *Nano Lett.*, 12(10):5122–5130, 2012.
- [44] J.C. Heyraud and J.J. Métois. Equilibrium shape and temperature; Lead on graphite. *Surface Science*, 128:334–342, 1983.
- [45] P. Hohenberg and W. Kohn. Inhomogeneous electron gas. *Phys. Rev.*, 136:B864–B871, Nov 1964.
- [46] J. Hwang, D. Campbell, S. Shivaraman, H. Alsalman, J. Y. Kwak, M. Kim, A. R. Woll, A. K. Singh, R. G. Hennig, S. Gorantla, M. H. Rummeli, and M. G. Spencer. Van der waals epitaxial growth of graphene on sapphire by CVD without a metal catalyst. *ACS Nano*, 7:385, 2013.
- [47] S. Ismail-Beigi and T. A. Arias. *Comp. Phys. Comm.*, 128:1, 2000.
- [48] Anubhav Jain, Shyue Ping Ong, Wei Chen, Bharat Medasani, Xiaohui Qu, Michael Kocher, Miriam Brafman, Guido Petretto, Gian-Marco Rignanese, Geoffroy Hautier, Daniel Gunter, and Kristin A. Persson. Fireworks: a dynamic workflow system designed for high-throughput applications. *Concurrency and Computation: Practice and Experience*, 2015.
- [49] Jin Joo, Hyon Bin Na, Taekyung Yu, Jung Ho Yu, Young Woon Kim, Fanxin Wu, Jin Z Zhang, and Taeghwan Hyeon. Generalized and facile synthesis of semiconducting metal sulfide nanocrystals. *Journal of the American Chemical Society*, 125(36):11100–5, sep 2003.
- [50] Ki Chul Kim, Bing Dai, J Karl Johnson, and David S Sholl. Assessing nanoparticle size effects on metal hydride thermodynamics using the Wulff construction. *Nanotechnology*, 20(20):204001, 2009.
- [51] Y. Kim, C. J. Cramer, and D. G. Truhlar. *J. Phys. Chem. A*, 113:9109, 2009.
- [52] Weon-Kyu Koh, Adam C. Bartnik, Frank W. Wise, and Christopher B. Murray. Synthesis of monodisperse pbse nanorods: A case for oriented attachment. *J. Am. Chem. Soc.*, 132(11):3909–3913, 2010.
- [53] W. Kohn. Nobel Lecture: Electronic structure of matterwave functions and density functionals. *Reviews of Modern Physics*, 71(5):1253–1266, oct 1999.

- [54] W Kohn, A D Becke, and R G Parr. Density Functional Theory of Electronic Structure. 0(96):12974–12980, 1996.
- [55] W. Kohn and L. J. Sham. Self-consistent equations including exchange and correlation effects. *Phys. Rev.*, 140:A1133–A1138, Nov 1965.
- [56] G. Kresse and J. Furthmüller. *Comput. Mater. Sci.*, 6:15–50, 1996.
- [57] G. Kresse and D. Joubert. From ultrasoft pseudopotentials to the projector augmented-wave method. *Phys. Rev. B*, 59:1758–1775, Jan 1999.
- [58] Nitin Kumar, Kevin Leung, and Donald J Siegel. Crystal surface and state of charge dependencies of electrolyte decomposition on limn2o4 cathode. *Journal of The Electrochemical Society*, 161(8):E3059–E3065, 2014.
- [59] Ravi Kumar, Sivakumar Pasupathi, Bruno G. Pollet, and Keith Scott. Nafion-stabilised platinum nanoparticles supported on titanium nitride: An efficient and durable electrocatalyst for phosphoric acid based polymer electrolyte fuel cells. *Electrochimica Acta*, 109(0):365 – 369, 2013.
- [60] Kendra Letchworth-Weaver and T. A. Arias. Joint density functional theory of the electrode-electrolyte interface: Application to fixed electrode potentials, interfacial capacitances, and potentials of zero charge. *Phys. Rev. B*, 86:075140, Aug 2012.
- [61] Elliott H Lieb and Barry Simon. The thomas-fermi theory of atoms, molecules and solids. *Advances in Mathematics*, 23(1):22 – 116, 1977.
- [62] J. Lischner and T. A. Arias. *J. Chem. Phys. B*, 114:1946, 2010.
- [63] Guozhen Liu, Erwann Luais, and J. Justin Gooding. The fabrication of stable gold nanoparticle-modified interfaces for electrochemistry. *Langmuir*, 27(7):4176–4183, 2011.
- [64] Tian-Fu Liu, Ying-Pin Chen, Andrey A. Yakovenko, and Hong-Cai Zhou. Interconversion between discrete and a chain of nanocages: Self-assembly via a solvent-driven, dimension-augmentation strategy. *Journal of the American Chemical Society*, 134(42):17358–17361, 2012. PMID: 23043458.
- [65] Yingying Lu, Zhengyuan Tu, and Lynden a. Archer. Stable lithium electrodeposition in liquid and nanoporous solid electrolytes. *Nature Materials*, 13(October):961–969, aug 2014.

- [66] K. Mathew and R. G. Hennig. VaspSol: Software module for solid/liquid interfaces for VASP, September 2013. <http://vaspsol.mse.cornell.edu/>.
- [67] K. Mathew and R. G. Hennig. VASPsol - Solvation model for the plane wave DFT code VASP. <https://github.com/henniggroup/VASPsol>, 2015.
- [68] Kiran Mathew, Ravishankar Sundararaman, Kendra Letchworth-Weaver, T. A. Arias, and Richard G. Hennig. Implicit solvation model for density-functional study of nanocrystal surfaces and reaction pathways. *The Journal of Chemical Physics*, 140(8):084106, 2014.
- [69] Carine Michel, Jérémie Zaffran, Agnieszka M Ruppert, Joanna Matras-Michalska, Marcin Jedrzejczyk, Jacek Grams, and Philippe Sautet. Role of water in metal catalyst performance for ketone hydrogenation: a joint experimental and theoretical study on levulinic acid conversion into gamma-valerolactone. *Chemical Communications*, 50(83):12450–12453, 2014.
- [70] Daniel F. Moyano and Vincent M. Rotello. Nano meets biology: Structure and function at the nanoparticle interface. *Langmuir*, 27(17):10376–10385, 2011.
- [71] C. B. Murray, , C. R. Kagan, and M. G. Bawendi. Synthesis and characterization of monodisperse nanocrystals and close-packed nanocrystal assemblies. *Annual Review of Materials Science*, 30(1):545–610, 2000.
- [72] Noel O’Boyle, Michael Banck, Craig James, Chris Morley, Tim Vandermeersch, and Geoffrey Hutchison. Open babel: An open chemical toolbox. *Journal of Cheminformatics*, 3(1):33, 2011.
- [73] Shyue Ping Ong, William Davidson Richards, Anubhav Jain, Geoffrey Hautier, Michael Kocher, Shreyas Cholia, Dan Gunter, Vincent L. Chevrier, Kristin A. Persson, and Gerbrand Ceder. Python Materials Genomics (pymatgen): A robust, open-source python library for materials analysis. *Computational Materials Science*, 68:314–319, 2013.
- [74] Jongnam Park, Kwangjin An, Yosun Hwang, Je-Geun Park, Han-Jin Noh, Jae-Young Kim, Jae-Hoon Park, Nong-Moon Hwang, and Taeghwan Hyeon. Ultra-large-scale syntheses of monodisperse nanocrystals. *Nature materials*, 3(12):891–5, dec 2004.
- [75] William D. Parker, John W. Wilkins, and Richard G. Hennig. Accuracy

- of quantum monte carlo methods for point defects in solids. *Phys. Status Solidi B*, 248(2):267–274, 2011.
- [76] Jayesh D. Patel, Frej Mighri, Abdellah Aji, and Tapas K. Chaudhuri. Morphology and size control of lead sulphide nanoparticles produced using methanolic lead acetate trihydratethiourea complex via different precipitation techniques. *Mater. Chem. Phys.*, 132(23):747 – 755, 2012.
- [77] J. P. Perdew, K. Burke, and M. Ernzerhof. *Phys. Rev. Lett.*, 77:3865, 1996.
- [78] S. A. Petrosyan, Jean-Francois Briere, David Roundy, and T. A. Arias. *Phys. Rev. B*, 75:205105, 2007.
- [79] S. A. Petrosyan, A. A. Rigos, and T. A. Arias. *J. Phys. Chem. B*, 109:15436–15444, 2005.
- [80] S. Plimpton. Fast Parallel Algorithms for Short Range Molecular Dynamics. *Journal of Computational Physics*, 117(June 1994):1–19, 1995.
- [81] John A. Pople, J. Stephen Binkley, and Rolf Seeger. Theoretical models incorporating electron correlation. *International Journal of Quantum Chemistry*, 10(S10):1–19, 1976.
- [82] George D. Purvis and Rodney J. Bartlett. A full coupledcluster singles and doubles model: The inclusion of disconnected triples. *The Journal of Chemical Physics*, 76(4), 1982.
- [83] R. D. Johnson III (ed.). Computational chemistry comparison and benchmark database. NIST Standard Reference Database Number 101, Release 16a, August 2012. <http://cccbdb.nist.gov/>.
- [84] K. Regan. *Science*, 295:2245, 2002.
- [85] Sung Sakong, Maryam Naderian, Kiran Mathew, Richard G Hennig, and Axel Groß. Density functional theory study of the electrochemical interface between a pt electrode and an aqueous electrolyte using an implicit solvent method. *The Journal of chemical physics*, 142(23):234107, 2015.
- [86] a. Santoro and a. D. Mighell. Coincidence-site lattices. *Acta Crystallographica Section A*, 29(2):169–175, 1973.

- [87] Paul Saxe, Henry F. Shaefer III, and Nicholas C. Handy. Exact solution (within a double-zeta basis set) of the schrodinger electronic equation for water. *Chemical Physics Letters*, 79(2):202 – 204, 1981.
- [88] Kathleen A. Schwarz, Ravishankar Sundararaman, Kendra Letchworth-Weaver, T. A. Arias, and Richard G. Hennig. Framework for solvation in quantum monte carlo. *Phys. Rev. B*, 85:201102, May 2012.
- [89] Kim A Sharp and Barry Honig. Calculating Total Electrostatic Energies with the Nonlinear Poisson-Bottzmann Equatlon. (9):7684–7692, 1990.
- [90] A. K. Singh and R. G. Hennig. Computational synthesis of single-layer GaN on refractory materials. *Appl. Phys. Lett.*, 105(5):051604, 2014.
- [91] Arunima K Singh, Richard G Hennig, Albert V Davydov, and Francesca Tavazza. Al₂O₃ as a suitable substrate and a dielectric layer for n-layer mos₂. *Applied Physics Letters*, 107(5):053106, 2015.
- [92] Arunima K. Singh, Kiran Mathew, Albert V. Davydov, Richard G. Hennig, and Francesca Tavazza. High throughput screening of substrates for synthesis and functionalization of 2d materials, 2015.
- [93] Arunima K. Singh, Kiran Mathew, Houlong L Zhuang, and Richard G Hennig. Computational screening of 2D materials for photocatalysis. *The Journal of Physical Chemistry Letters*, 6(6):1087–1098, 2015.
- [94] Arunima K. Singh, Houlong L. Zhuang, and Richard G. Hennig. Ab initio synthesis of single-layer III-V materials. *Physical Review B*, 89:245431, Jun 2014.
- [95] R. Sundararaman, D. Gunceler, K. Letchworth-Weaver, and T. A. Arias., 2012.
- [96] Ravishankar Sundararaman and T.A. Arias. Efficient classical density-functional theories of rigid-molecular fluids and a simplified free energy functional for liquid water. *Computer Physics Communications*, 2013. (in print).
- [97] J. Tomasi, B. Mennucci, and R. Cammi. *Chem. Rev.*, 105:2999, 2005.
- [98] Thanh N. Truong and Eugene V. Stefanovich. Hydration effects on reac-

- tion profiles: an ab initio dielectric continuum study of the $\text{Sn}^{2+} + \text{CH}_3\text{Cl}$ reaction. *J. Phys. Chem.*, 99(40):14700–14706, 1995.
- [99] Agnieszka Tymosiak-Zieliska and Zofia Borkowska. Double layer capacitance of Pt(111) single crystal electrodes. *Electrochimica Acta*, 46:3063–3071, 2001.
- [100] D. Vanderbilt. *Phys. Rev. B*, 41:7892, 1990.
- [101] W. Kohn; L. J. Sham. Self-Consistent Equations Including Exchange and Correlation Effects. 385(1951), 1965.
- [102] Deli Wang, Huolin L. Xin, Yingchao Yu, Hongsen Wang, Eric Rus, David A. Muller, and Hector D. Abrua. Pt-decorated PdCo@Pd/C core-shell nanoparticles with enhanced stability and electrocatalytic activity for the oxygen reduction reaction. *J. Am. Chem. Soc.*, 132(50):17664–17666, 2010.
- [103] Xiaoping Wang, Romesh Kumar, and Deborah J. Myers. Effect of Voltage on Platinum Dissolution. *Electrochemical and Solid-State Letters*, 9(5):A225, 2006.
- [104] Andrew A R Watt, David Blake, Jamie H Warner, Elizabeth A Thomsen, Eric L Tavenner, Halina Rubinsztein-Dunlop, and Paul Meredith. Lead sulfide nanocrystal: conducting polymer solar cells. *J. Phys. D: Appl. Phys.*, 38(12):2006, 2005.
- [105] Jody A White, Eric Schwegler, Giulia Galli, and François Gygi. The solvation of Na^+ in water: First-principles simulations. *Journal of Chemical Physics*, 113(11), 2000.
- [106] Houlong L Zhuang, Arunima K. Singh, and Richard G Hennig. Computational discovery of single-layer III-V materials. *Physical Review B*, 87(16):165415, 2013.
- [107] A Zur and TC McGill. Lattice match: An application to heteroepitaxy. *Journal of applied physics*, 55(2):378–386, 1984.